ACCELERATING MRI IMAGING USING ADVANCED COMPRESSED SENSING TECHNIQUES

BY

Murad Almadani

A Thesis Presented to the

DEANSHIP OF GRADUATE STUDIES

KING FAHD UNIVERSITY OF PETROLEUM & MINERALS

DHAHRAN, SAUDI ARABIA

In Partial Fulfillment of the
Requirements for the Degree of

MASTER OF SCIENCE

In

ELECTRICAL ENGINEERING

April, 2019

KING FAHD UNIVERSITY OF PETROLEUM & MINERALS

DHAHRAN- 31261, SAUDI ARABIA

DEANSHIP OF GRADUATE STUDIES

This thesis, written by **Murad Almadani** under the direction of his thesis advisor and approved by his thesis committee, has been presented and accepted by the Dean of Graduate Studies, in partial fulfillment of the requirements for the degree of **MASTER OF SCIENCE IN ELECTRICAL ENGINEERING.**

Dr. Mudassir Masood
(Advisor)

Dr. Abdallah Al-Ahmari
Department Chairman

Dr. Azzedine Zerguine
(Member)

Dr. Salam A. Zummo
Dean of Graduate Studies

Dr. Tareq AlNafouri
(Member)

21/4/19

Date: April 1, 2019

Dedication

Dedicated to my great and sacrificer mother WAFAA ALSHEKHA who always gives her best to support me, and to my educator and virtuous father MOHAMMAD EID who has passed away during this degree completion (may Allah grants him the highest level of paradise)

ACKNOWLEDGMENTS

In the name of Allah the Merciful the most gracious

Firstly, all thanks and praises to almighty Allah for inspiring me the patience and encouragement to successfully complete this research work. Then I would like to express my gratitude and appreciation to my advisor Dr. Mudassir Masood for his guidance and wise advices he had given me, and the numerous times of attention devoted throughout this research work. Also, the thanks are due to King Fahd University of petroleum and minerals (KFUPM), especially, the Electrical Engineering department who have given me the opportunity to conduct this research.

My sincere thanks also go to my thesis committee members Dr. Azzedine Zerguine and Dr. Tareq AlNaffouri who gave thoughtful comments and reviewed my work on a very short notice.

Finally, I would not forget to thank my colleagues and friends, especially my roommate (Mohammad Aljawhary), Mohammad Altakrouri, Elmobarak Emam, Sidqy Alnajar, Sagiru Gaya, and many others whom I will not be able to name here, for helping me to pass hard and critical moments during my staying in KFUPM campus.

TABLE OF CONTENTS

LIST OF TABLES

LIST OF FIGURES

LIST OF ABBREVIATIONS

MRI	:	Magnetic Resonance Imaging
CS	:	Compressed Sensing
CSC	:	Convolutional Sparse Coding
DL	:	Dictionary Learning
LoBCoD	:	Local block coordinate descent
FDLCP	:	Fast Dictionary Learning on Classified Patches
ADMM	:	Alternating Direction Method of Multipliers
TV	:	Total Variation
PSNR	:	Peak Signal to Noise Ratio
RLNE	:	Relative L_2 Norm Error
PSLR	:	Peak Side-Lobe Ratio
PSF	:	Point Spread Function
FSE	:	Fast Spin Echo
GE	:	Gradient Echo
$\mathbf{G_{PE}}$	:	Phase Encode Gradient
$\mathbf{G_{FE}}$	:	Frequency Encode Gradient

$\mathbf{G_{SS}}$: Slice Selection Gradient

ABSTRACT

Full Name : [MURAD (MOHD EID) HAMZEH ALMADANI]

Thesis Title : [ACCELERATING MRI IMAGING USING ADVANCED COMPRESSED SENSING TECHNIQUES]

Major Field : [Signal Processing]

Date of Degree : [April 2019]

Compressed sensing has been widely used in recent literature to reduce the scanning time in MRI. Incoherently subsampling the data in K-space is the core of MRI compressed sensing which causes noise like artefacts in image domain, that can be removed using image recovery process. In MRI images, as most of the energy is concentrated around the center of K-space, incoherent sub-sampling using the most commonly used Cartesian trajectory will result in sub-standard performance. Radial trajectory has been proposed earlier to solve this problem, since it samples the center of K-space without compromising the incoherence. However, due to strict operational requirements and computational processes, radial trajectory is rarely used in real MRI scanners. In this research work, a newly developed trajectory is proposed, that surpasses the performance of the Cartesian trajectory while preserving the same level of executional simplicity. Extensive simulations have been performed to demonstrate the superiority of the proposed trajectory on static MRI imaging using MRiLab toolbox and FDLCP reconstruction algorithm. On the other hand, the-state-of-the art CS-MRI reconstruction algorithm is relying on patch-based dictionary learning techniques. Such techniques fail to detect global image features, which negatively reflects on the reconstruction accuracy. Consequently, in this research work, we

have also introduced a novel algorithm based on convolutional sparse coding which results with Worthwhile MRI image reconstruction accuracy.

Keywords—Magnetic resonance imaging (MRI), compressed sensing (CS), Cartesian trajectory, radial trajectory, MRiLab toolbox, patch-based dictionary learning, convolutional sparse coding.

ملخص الرسالة

الاسم الكامل: مراد (محمد عيد) حمزة المدني

عنوان الرسالة: تسريع التصوير بالرنين المغناطيسي باستخدام تقنيات استشعار الضغط المتقدمة

التخصص: معالجة الإشارات

تاريخ الدرجة العلمية: أبريل 2019

تم استخدام تقنية الاستشعار المضغوط على نطاق واسع في الأدبيات الحديثة لتقليل وقت المسح في التصوير بالرنين المغناطيسي. إن أخذ البيانات الموجودة في K-space بشكل غير مترابط هو جوهر هذه التقنية والذي يسبب تشويش في مجال الصورة ، والتي يمكن إزالتها باستخدام عمليات استرداد الصورة. في صور التصوير بالرنين المغناطيسي ، حيث أن معظم الطاقة تتركز حول مركز K-space ، فإن أخذ العينات الفرعية غير المتماسكة باستخدام المسار الديكارتي الأكثر استخدامًا سيؤدي إلى أداء دون المستوى. تم اقتراح مسار شعاعي في وقت سابق لحل هذه المشكلة ، لأنه يأخذ عينات من مركز K-space دون المساس بعدم الاتساق. ومع ذلك ، نظرًا لمتطلبات التشغيل الصارمة والعمليات الحسابية ، نادرًا ما يستخدم المسار الشعاعي في ماسحات التصوير بالرنين المغناطيسي الحقيقية. في هذا العمل البحثي ، تم اقتراح مسار تم تطويره حديثًا ، والذي يتجاوز أداء المسار الديكارتي مع الحفاظ على نفس المستوى من البساطة التنفيذية. تم إجراء عمليات محاكاة واسعة النطاق لإظهار تفوق المسار المقترح على التصوير بالرنين المغناطيسي الثابت باستخدام أدوات MRiLab وخوارزمية إعادة بناء FDLCP. من ناحية أخرى ، تعتمد خوارزمية إعادة إعمار CS-MRI الحديثة على تقنيات تعلم القاموس القائم على التصحيح. تفشل مثل هذه التقنيات في اكتشاف ميزات الصور الكليَة ، والتي تنعكس سلبًا على دقة إعادة الإعمار. وبالتالي ، في هذا العمل البحثي ، قدمنا أيضًا خوارزمية جديدة تستند إلى تشفير تلافيفي متقطع ينتج عنه دقة جديرة بالاهتمام لإعادة بناء صورة التصوير بالرنين المغناطيسي.

CHAPTER 1

INTRODUCTION

1.1 Motivation

Magnetic Resonance Imaging (MRI) is an important non-ionizing three-dimensional medical imaging technique. As compared to other imaging methods (e.g. computed tomography, positron emission tomography, Single-photon emission computed tomography), MRI has superior performance in imaging soft tissues and detecting many physiological and pathological aspects of organs such as blood flow, heart contraction and relaxation procedures. Although it is superior in image quality, MRI needs the longest acquisition time as compared to other imaging techniques.

Unlike most of the three-dimensional imaging techniques, MRI samples the data of interest in the frequency domain, which is usually called K-space domain. In MRI terminology, three main orthogonal magnetic gradients are used to determine the location in the K-space that has to be sampled. The scanning is performed in a slice-by-slice manner. One of these gradients is responsible to select a two-dimensional plane (slice) to be sampled. Therefore, we call it slice selection gradient G_{SS}. The remaining two gradients control the way the data is sampled from the selected slice. We call these gradients the frequency encoding G_{FE} and phase encoding gradients G_{PE}. There are three principal approaches to sample data from

2D slices by manipulating these gradients. The resultant sampling pattern is called K-space trajectory.

The most commonly used trajectory is the Cartesian trajectory. In this trajectory, the K-space data is sampled row-by-row by changing the value of G_{PE} each time, while maintaining G_{FE} values. As long as G_{PE} and G_{SS} are guaranteed to be operated before G_{FE}, the exact timing of the application of gradients is not important. This simple procedure makes the Cartesian trajectory the most commonly used trajectory in MRI scanners these days.

The second important trajectory is the radial trajectory. In this trajectory, G_{PE} and G_{FE} operate simultaneously with different amplitudes to form the full K-space data in a radial fashion. Radial trajectory samples the center of the K-space in a much better way as compared to the Cartesian trajectory. This kind of procedure makes the radial trajectory more robust than the Cartesian trajectory, since most of the energy in K-space is concentrated around its center. However, this trajectory suffers due to a strict requirement of synchronization between the theoretical and actual timing of the gradients. An improper synchronization will result in an effect called gradient delay effect. This appears in the form of a streak artefact in real image domain. Countering this effect is expensive and requires repetitive recalibration [1,2].

The third important trajectory that has been used in MRI K-space formation is the spiral trajectory. Like the radial trajectory, the spiral trajectory operates G_{PE} and G_{FE} at the same time. Using sinusoidally increasing amplitudes and 90^{o} phase shifts between the gradients, the data will be detected in a spiral fashion. The spiral shape allows this trajectory to sample

the whole K-space data at once. This makes it the fastest trajectory among the rest, however, with lowest image quality. Spiral trajectory is used mainly in applications where quick scanning is more important than image quality (e.g. functional MRI).

Reducing the scanning time while preserving good image quality is still an open problem in MRI. One possible way to tackle this problem is to reduce the number of samples to be scanned in the K-space using either Cartesian or radial trajectory via compressed sensing [3]. In conventional undersampling procedure, the resultant image could suffer from bad resolution. However, according to the compressed sensing theory, if the image to be sampled is sparse in some domain, and it can be sampled incoherently, then the original image can be reconstructed from a very small number of its samples without significant compromise on its quality [4,5].

Undersampling K-space incoherently using row-by-row Cartesian trajectory would fail to capture a large part of K-space energy as most of the K-space energy is concentrated around its center. In order to tackle this issue, increasing the number of samples around the center of K-space, while decreasing the samples far beyond its center is a possible solution [6,7]. However, such solution will result in two fundamental problems. First, we will lose some incoherence, therefore, the performance of compressed sensing recovery will be affected [8]. Secondly, less samples away from the origin means less high frequency data, which would again affect the quality of the reconstructed image. Undersampling using radial trajectory may solve the problem; however, it requires high computational cost as discussed earlier [1].

The authors in [9] proposed a four-shot 2D sinusoidal trajectory. This trajectory solves the incoherence issue and at the same time provides significant high-speed scanning as it utilizes only four MR excitations. However, this approach suffers from eddy currents produced due to the sinusoidally changing shape of the gradient amplitude. This imposes additional computational burden for image construction [10].

A masking based approach appears in [11], where the authors have proposed a circular version of Cartesian trajectory claiming that it mimics the radial sampling fashion. In this approach, the full-sampled K-space data is simply multiplied by the corresponding trajectory mask. We believe that the solution proposed in this paper does not solve the problem as it still requires a full sampled K-space, that can only be achieved through regular scanning using the traditional Cartesian trajectory. Finally, to the best of our knowledge, no trajectory has been proposed in the literature that provides higher incoherence and at the same time simple to implement.

In this research work, we propose a new trajectory that allows us to capture higher K-space energy, while preserving sufficient incoherence. The proposed trajectory also enjoys the simplicity offered by Cartesian trajectory and, therefore, lends itself to easier incorporation in real MRI scanners.

Moreover, the trendy CS MRI technique is relying on algorithms work on image patches [12], which loss to detect MRI global image features in reconstruction process, which is important in imaging diagnosis. Convolutional sparse coding (CSC) approach has been proposed recently to overcome this issue with better image reconstruction accuracy. However, the Contemporary attempts rely on ADMM algorithm [13] which suffers from

its many regularization parameter that are application dependent [14]. In this work, we are going to implement CSC model in MRI image reconstruction dispensing with ADMM approach, by introducing other technique called LoBCoD algorithm [15].

1.2 Objectives of the Research

In this research work, we are aiming to propose:

- A new trajectory that solve the incoherence problem of the Cartesian trajectory in CS subsampling enjoying the same level of simplicity.
- A novel reconstruction algorithm based on CSC model, such that, it leads for higher reconstruction accuracy than the state-of-the-art patch-based dictionary learning algorithms.

1.3 Thesis Outline

The rest of the thesis is organized as follows. In chapter 2, we briefly review the prior work and background on MRI CS. The proposed K-space trajectory is presented in chapter 3 with its experimental results, and chapter 4 shows the proposed reconstruction algorithm along with its experimental results. Finally, we conclude and discuss possible future directions in chapter 5.

CHAPTER 2

BACKGROUND AND PRIOR WORK

2.1 MRI Physics

Unlike other three-dimensional imaging techniques, MRI has a unique execution procedure with ability to create hundreds of images from different directions. This could be done by simply adjusting the gradient magnetic fields. The following sub-sections demonstrate the MRI execution procedure in detail.

2.1.1 Image Formation

The magnetic dipole formation of the proton spinning behavior is the core idea of MRI imaging formation. Most of the human body mass are containing of hydrogen atoms which is consisting of one proton in its nuclei. This proton is spinning in nature which resultants with magnetic dipole due to its positive charge. The random orientations of all the atoms in human body cancels the effect of these magnetic dipoles with almost zero magnitude in resultant. MRI scanner contains a huge magnetic field which aligns these magnetic dipoles in its direction which cause the proton atoms to precess around the main magnetic field line with angular frequency related to the main magnetic field strength. This angular frequency called the Larmor frequency as describe in equation (1) and shown in Figure 1.

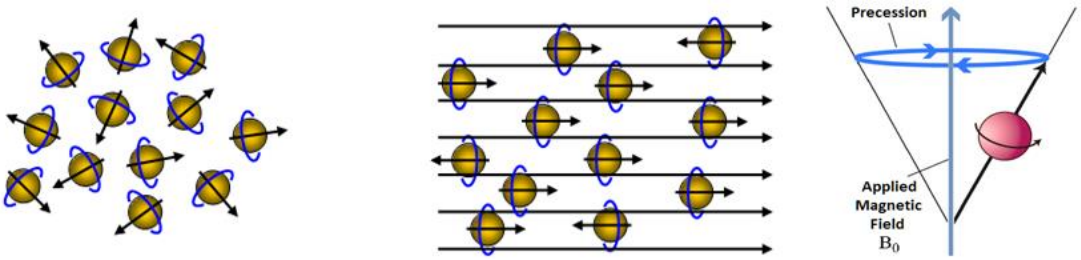

Figure 1 Proton alignment and Precession [16].

$$w_{Larmor} = \gamma B_0 \tag{1}$$

where γ is a constant and B_0 is the magnetic field strength in Tesla. However, the key point of understanding the formation of MRI images is to know that, the formation of these images occurred in frequency domain, which depending on the Larmor frequency that operate each atom in the targeted area at the scan time. In order to get a signal form these atoms, an excitation process must perform using radio frequency transmitters that emits RF signal with frequency equal to the Larmor frequency to guarantee the resonance. And as it can be seen from (1), the Larmor frequency is mainly depending on the strength of the magnetic field, that inspired the idea of slice selection gradient which applies dynamic magnetic field that makes the strength of the magnetic field changes along certain direction. This changing in magnetic field strength makes the Larmor frequency varies along that direction, which makes it possible to excite certain thickness slice of the body once at a time, as shown in Figure 2.

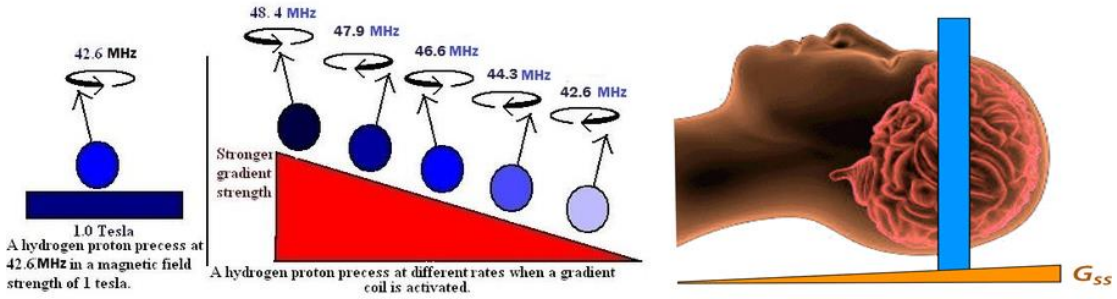

Figure 2 Slice selection gradient [17].

After selecting the slice to be sampled, and in order to construct all the frequencies in the K-space of that particular slice, phase encoding gradient and frequency encoding gradient must apply in orthogonal directions. Assigning different values of the phase and frequency encodes with different timing will result with detecting the whole K-space data. A receiver coil must be replaced near the targeted area to detect the radio frequency signal produced by releasing the energy stored in the protons in the excitation process. The detected signal contains different energies and frequencies depending on the proton concentration and certain characteristics of tissues in the body to form useful information in K-space domain. The following equations describes the previous discussion:

$$M(x,y,z) = M_0 + xG_x + yG_y + zG_z \tag{2}$$

This equation describes the magnetic field strength in every location of the targeted area, where M_0 is the main magnet and the G_x, G_y, G_z are to be assigned as phase, frequency and slices selection gradients. the RF signal detected in certain voxel in certain time is defined by:

$$r(x,y,t) = f(x,y)e^{j\Phi(t)} \tag{3}$$

where $f(x,y)$ is the spatial domain of MRI images, and $\Phi(t)$ is the phase angle of the protons inside that voxel which depends on the applied frequency and phase gradients in that particular slice, as described by:

$$w = \gamma B(x,y,t) = \frac{d\Phi(t)}{dt}$$

$$\Phi(t) = \int_0^t \gamma B(x,y,t) d\tau$$

$$\Phi(t) = \int_0^t \left(\gamma B_0 + x\gamma G_x(\tau) + y\gamma G_y(\tau)\right) d\tau$$

$$\Phi(t) = w_{Larmor} t + xK_x(t) + yK_y(t) \tag{4}$$

Using the definition of equation (1), the phase $\Phi(t)$ has been calculated in equation (4), where $K_x = \int_0^t \gamma G_x(\tau) d\tau$ and $K_y = \int_0^t \gamma G_y(\tau) d\tau$ are equal to the values of K-space matrix.

Substituting the value of $\Phi(t)$ into (3), the RF signal detected will be:

$$r(t) = f(x,y) e^{jw_{Larmor}t} e^{j(xK_x(t)+yK_y(t))} \tag{5}$$

where $e^{jw_{Larmor}t}$ is the carrier of the cardinal sine function of the RF signal.

Therefore, if we want to derive the RF signal of the whole slice from the single voxel $r(t)$, an integral operation taken for equation (5) describes as follow:

$$R(t) = e^{jw_{Larmor}t} \iint f(x,y) e^{j(xK_x(t)+yK_y(t))} \, dxdy \tag{6}$$

where $R(t)$ is the whole RF signal detected from single slice. And if we assume the $K_x(t)$ and $K_y(t)$ to be the Fourier domain axises of MRI image, the $R(t)$ will be equal to the Fourier transform of $f(x, y)$.

So, depending on the result we got in equation (6), the formation of K-space in MRI occurs when $K_x \; and \; K_y$ change their values during the relaxation process. Which means that in order to collect the whole K-space data we must change the corresponding phase and frequency encodes values in each excitation for each detected slice. Finally, and after we detect the whole K-space data, we perform an inverse Fourier transform to calculate the spatial domain image values $f(x, y)$.

2.1.2 MRI Sequences

In conclusion of the previous section, in order to construct a full one slice MRI image, we must operate multiple gradients and RF transmitted signals in different times and amplitudes. This kind of procedure are conventionally known as MRI sequences.

One of the most famous and commonly used sequences in MRI is the gradient echo sequence (GRE), as describe in Figure 3, an RF transmitter operate with the same time of slice selection gradient to excite single slice at a time. After that and in the direction of the phase encoding gradient, multiple values have to be operated to form row by row sorting of the data in K- space domain. Finally, a frequency encoding gradient operate with equally amplitudes in each time at the instance of reading the signal by the receiver coils, that makes the frequency encoding gradient named as a readout gradient.

We also can notice the negative values in the direction of slice selection and readout gradients. These negative gradient values prevent the dephasing between the precessing

atoms at the reading stage, which helps to detect the highest energy possible to form the K-space values.

The GRE sequence is able to differentiate between different types tissues using the time relaxation property of protons called T1. Every tissue in any part of the body has a unique relaxation time after the excitation process, which makes some of tissues to have long relaxation time which makes the energy of the emitted signal last longer than others, and by adjusting the readout time (TE) along with the repetition time (TR) properly, a high resolution T1 weighted MRI image can be constructed.

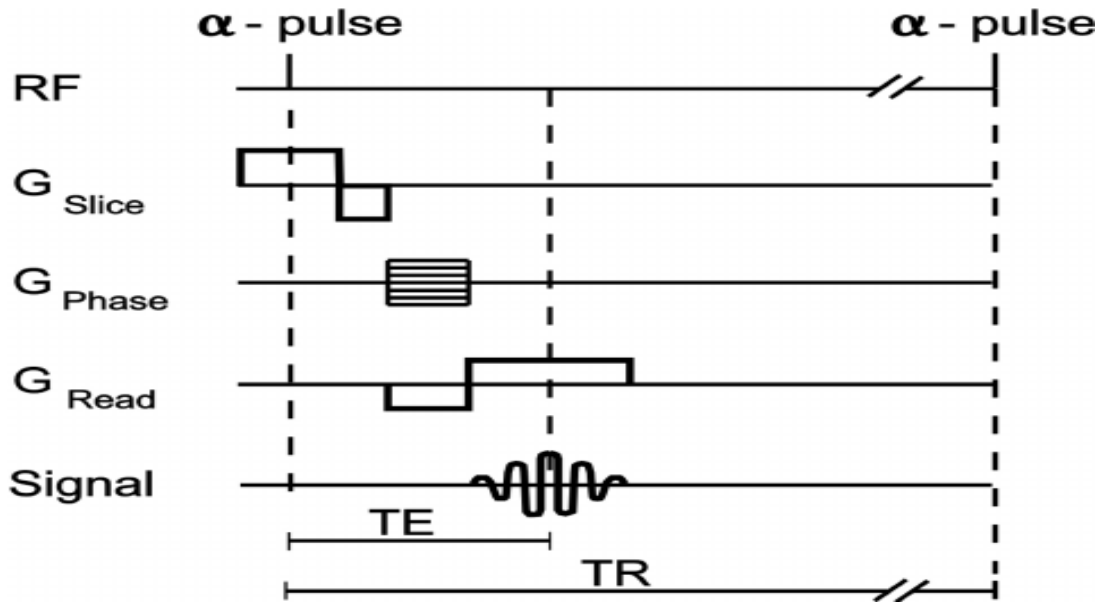

Figure 3 Gradient Echo Sequence [18].

The magnetic inhomogeneity is one of the most common problem in real MRI scanner, this inhomogeneity effects the Larmor frequency of the excited part of the body causing dephasing behavior in the precessing protons, which makes the signal to vanish faster than it should be. This problem is solved using spin echo sequence (SE), by exciting the targeted area using 180^0 RF pulse which invert the dephasing until the rephrasing occurs at the

readout instant. Fortunately, this dephasing time is a unique tissues property, which make it the second tissue property that can be used to differentiate between tissues in the image and increase the resolution, which called T2 weighted MRI images.

In order to get T2 contrast image using SE sequence, a very high value of TE and TR is chosen along with using 180^0 RF pulse in every excitation. This results with very slow scanning time making this sequence not preferable to be used. Fast spin echo sequence is the accelerated version of the SE sequence, which detect multiple RF signals with multiple phase encoding values in one excitation process, as shown in Figure 4.

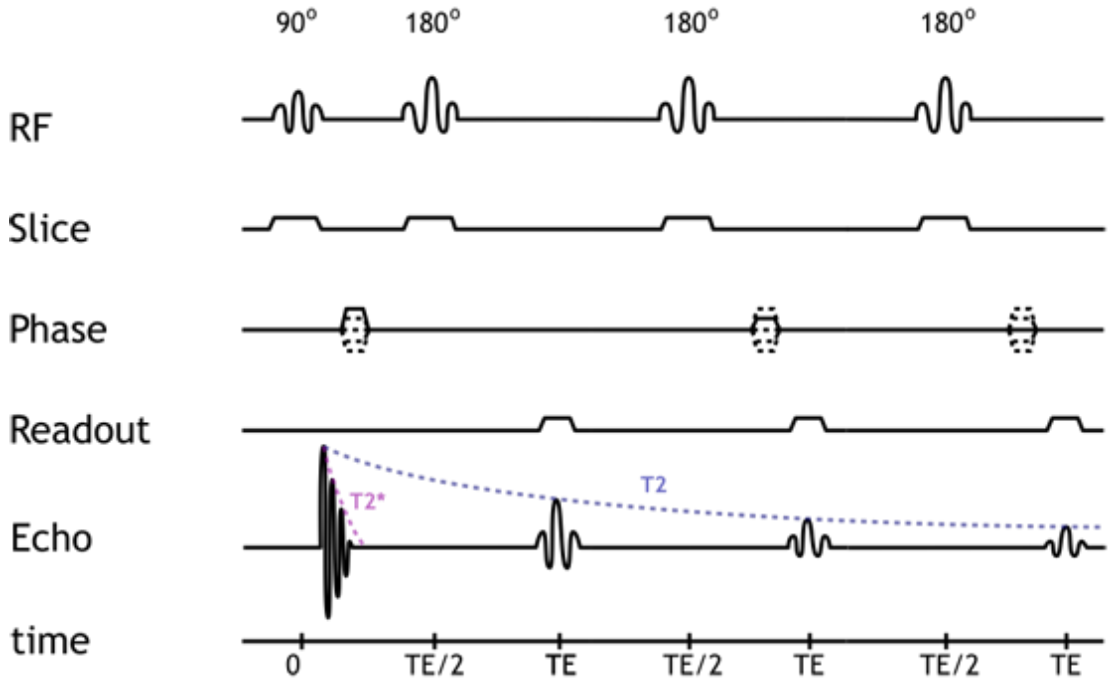

Figure 4 Fast Spin Echo Sequence [19].

2.1.3 K-space Trajectories

As discussed earlier, the timing and the amplitude of applying the orthogonal gradients will decide the sorting behavior of the K-space data in the readout process. There are three main

sorting types of the K-space data, which are called the Cartesian, radial and spiral K-space trajectories, as shown in Figure 5. In the cartesian trajectory, the slice selection and the phase encoding gradients operate before the readout step, which cause the data in K-space sorting in row-wise, without synchronizing demanding between any of the gradients, which makes it the most easy and common trajectory used in real MRI scanners.

Most of MRI images data energy is located around the center of K-space domain, as shown in Figure 6. This property of the K-space inspired the idea of radial trajectory. The radial trajectory has the ability to sample the center of K-space more efficient than the row-by-row Cartesian. This can be done by operating the phase and frequency encoding gradients at the same instant with different amplitudes in each excitation procedure. This synchronization behavior of the gradients makes the radial trajectory affected by the gradient delay effect, as shown in Figure 7, which required more computation and calibration burdens to overcome, which makes this trajectory inapplicable in real MRI scanner and make it the least commonly used.

The third K-space trajectory is the spiral trajectory which has the minimum execution time among the others. Detecting K-space data using This trajectory can be done by applying the phase and frequency encodes with increasingly sinusoidal amplitudes. This procedure has the ability to detect the whole K-space data in single excitation. Upon this, the spiral trajectory is commonly used in imaging that required fast detecting for certain tissue behavior regardless of the resolution of the image, like in Functional MRI application.

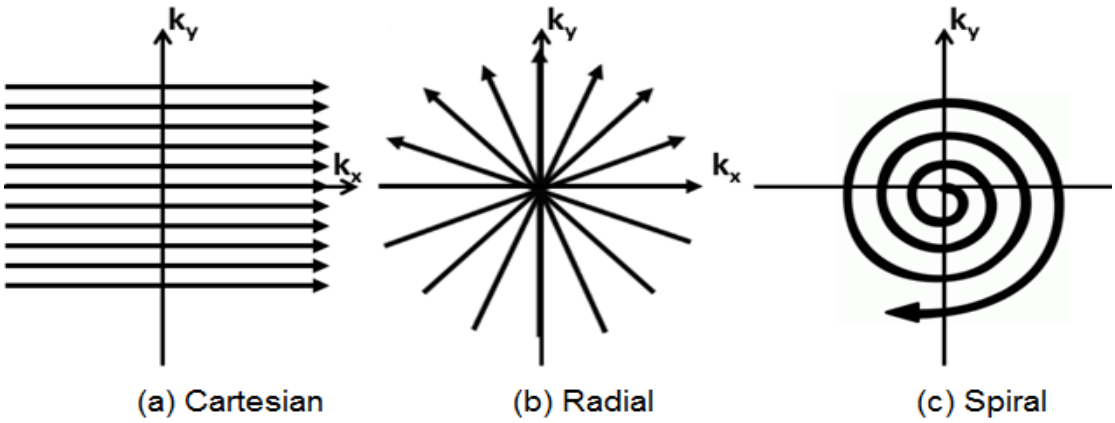

Figure 5 Different types of K-space trajectories in MRI [20].

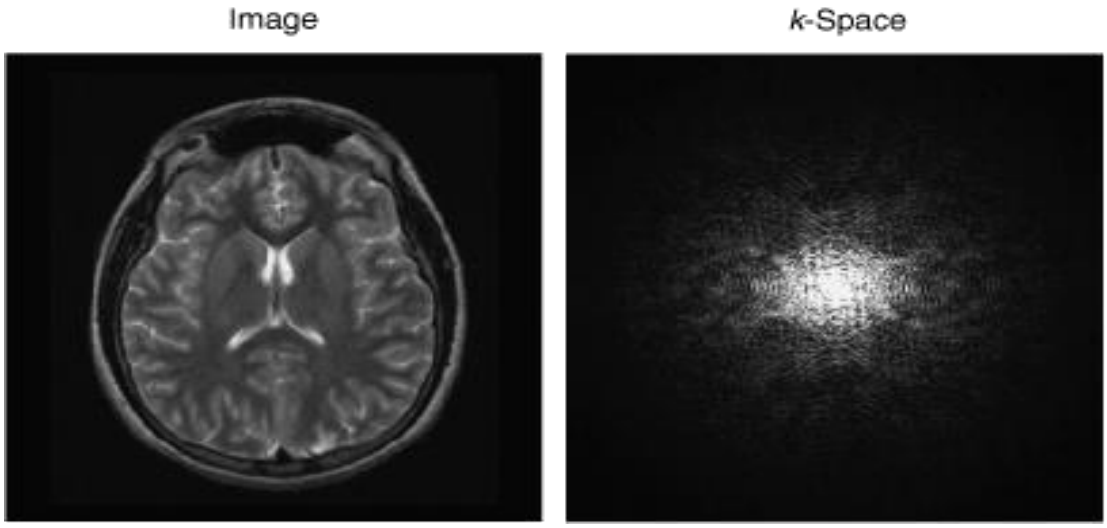

Figure 6 Sample MRI image and K-space data [21].

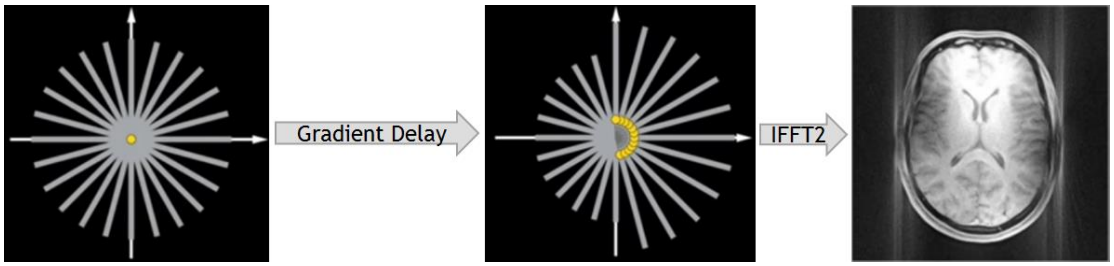

Figure 7 Gradient delay effect (streak artefact) on real brain image using radial trajectory.

2.2 MRI and Compressed Sensing

Accelerating MRI imaging without compromising its imaging quality remains a challenge, especially for patients who are anxious and cannot keep still and for those who have limited breath hold capacity. These challenges can be solved with compressed sensing, the technology that helps us to go beyond speed by drastically decreasing acquisition times in MRI without sacrificing image quality. In traditional MRI scanner, we would sample all raw data point of MRI images in K-space domain. This guarantees the highest image quality we can think of, but this also makes MRI scans long. However, compressed sensing changes the game based on three golden rules, incoherent subsampling, transform sparsity and non-linear iterative reconstruction.

In currently existing acceleration techniques, we sample just a part of the raw data points. However, subsampling typically is accompanied by a degradation of image quality, for example, either low resolution image or an image with folding artefact. At this point, incoherence comes into the picture. Incoherent sampling means that the data points are sampled randomly. Instead of having distinct aliasing artefacts as evident in conventional undersampling, incoherent subsampling leads to noise like artefacts, which can be removed by assuming sparsity in certain domain.

An image is considered sparse when its informational content is reflected in as few data points as possible. A good example of an MRI image exhibiting sparsity is from angiography. In angiography images, the data of interest is sparse in spatial domain, which is represented by white vessels that are surrounded by a black background. Although the background is often not exactly black, but no important information is lost by setting the background data to zero. Like other natural images, most MRI images are sparse in wavelet

domain. Taking advantage of incoherent subsampling, much of the noise can be taken care of by thresholding the image in its transform sparsity (wavelet) domain. This makes the image clearly improved when we transform it back to its original representation, as described in Figure 8. Mathematically, the whole process can be achieved by solving the following optimization problem:

$$\min_{\mathbf{x}} \|\mathbf{F_u x} - \mathbf{y}\|_2^2 + \lambda \|\mathbf{\Phi x}\|_0 \quad (7)$$

where $\mathbf{x}$ is the reconstructed image, $\mathbf{\Phi}$ is any suitable sparsifying transform matrix, $\mathbf{y}$ is the measured K-space data, $\mathbf{F_u}$ is the undersampled Fourier transform, and λ is the regularization parameter. The first term of the equation ensures data consistency, while the other term forces the transform sparsity. Many algorithms have been proposed to approximate this NP-Hard problem. In [22], the authors have converted the problem into convex by relaxing the l_0 norm of the sparse representation term into l_1 norm. They found the solution using conjugate gradient descent algorithm, assuming sparsity in Wavelet and Total Variation (TV) domains, while Contourlet domain has been used in [23].

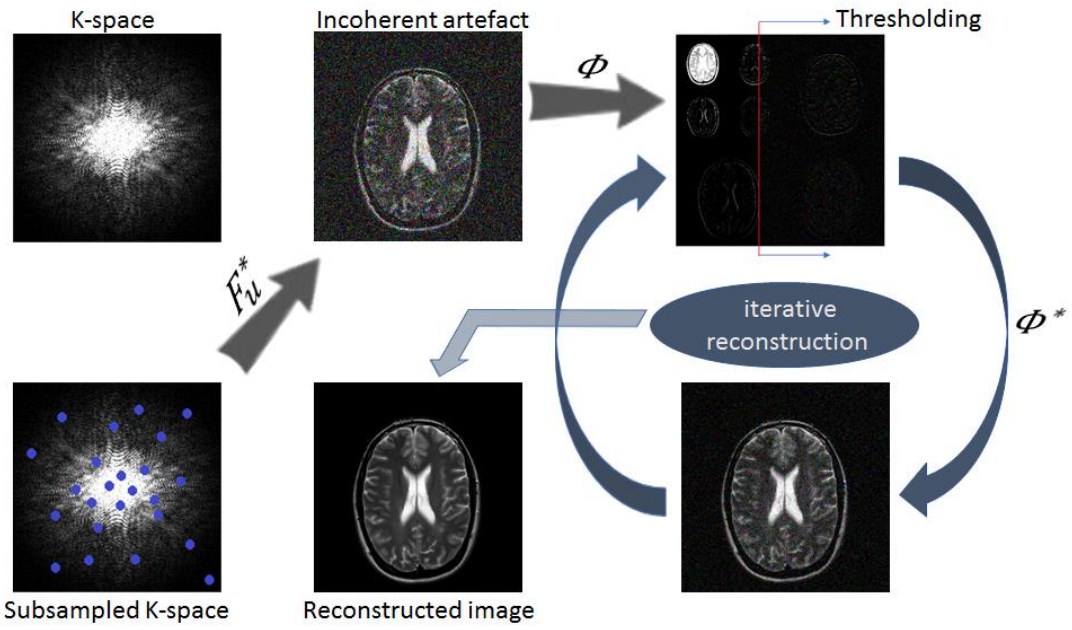

Figure 8 General description of MRI CS and its three golden rules: transform sparsity, incoherent subsampling and the non-linear iterative reconstruction that balances between the data consistency and the transform sparsity. Where, F* and Φ* indicate the inverse Fourier and wavelet operations respectively.

Searching for better representative dictionaries has been drawing considerable attention in recent years. Specifically, patch-based dictionary learning approach has been applied on MRI CS problem in [12] by splitting the problem into two main parts, as explained next.

The first part is to learn the sparsifying dictionary using certain number of overlapping image patches, along with its sparse representations by solving the following optimization problem:

$$\min_{\mathbf{D},\boldsymbol{\alpha}_{ij}} \sum_{ij} \left\| \mathbf{R}_{ij}\mathbf{x} - \mathbf{D}\boldsymbol{\alpha}_{ij} \right\|_2^2 \quad s.t. \left\| \mathbf{d}_k \right\|_2 = 1 \quad \forall k, \ \left\| \boldsymbol{\alpha} \right\|_0 < T_0 \quad \forall i,j, \tag{8}$$

where $\mathbf{D}$ is the learned dictionary, $\mathbf{R}_{ij}$ is the patch extracting operator, and $\boldsymbol{\alpha}_{ij}$ is the sparse representation for each image patches. This can be solved using K-SVD algorithm [24] to learn the dictionary, along with sparse coding to find the sparse representations α_{ij}.

After learning the dictionary and finding the sparse representations, the reference image is updated by solving the following quadratic term, that forces the data consistency of the final solution with respect to the acquired data as occurred in equation (7):

$$\min_{\mathbf{x}} \sum_{i,j} \left\| \mathbf{R}_{ij}\mathbf{x} - \mathbf{D}\boldsymbol{\alpha}_{ij} \right\|_2^2 + \frac{\nu}{2} \|\mathbf{F_u}\mathbf{x} - \mathbf{y}\|_2^2 \quad (9)$$

While, the resultant image will be reconstructed after doing certain number of iterations between these two steps.

Although the result of this approach gains more interests with respect to the result gained by [22] with fixed dictionary, but it losses the relationship between the image patches ,therefore, it may fail to detect global image features, which it is very important in MRI images.

CSC is a new learning-based sparse representation technique that represent the input image by summation of sparse feature maps (with the same image size) convolved with kernels that are small in size (compare to the input image). Such kernels will operate globally on sparse feature maps, which overcomes the miscarrying of important image features that occurs in patch-based learning approach. Let m be the filters number, $\mathbf{d}_k$ is a filter of size $\sqrt{n} \times \sqrt{n}$, and $\mathbf{z}_k$ is its corresponding sparse feature map. Quan and Jeong [14] implemented CSC model to reconstruct undersampled MRI images by solving the following:

$$\min_{\mathbf{d},\mathbf{z},\mathbf{x}} \frac{\tau}{2} \|\mathbf{x} - \sum_{k=1}^{m} \mathbf{d}_k * \mathbf{z}_k\|_2^2 + \lambda \sum_{k=1}^{m} \|\mathbf{z}_k\|_1 \quad s.t. \ \|\mathbf{F_u}\mathbf{x} - \mathbf{y}\|_2^2 < \varepsilon \ , \|\mathbf{d}_k\|_2^2 \leq 1 \quad (10)$$

where $*$ is the convolutional operation between the kernels and its corresponding sparse feature maps. Such a problem is generally non-convex and finding its optimum solution is

not guaranteed. However, inspired by the solution provided by ([25,26,27]), they used ADMM to overcome this issue, by dividing the whole problem into many subproblems, trying to find the optimum solution in an iterative manner, which convert the general equation into:

$$\min_{\mathbf{d},\mathbf{x},\mathbf{g},\mathbf{z},\mathbf{s}} \frac{\tau}{2}\left\|\mathbf{x}-\sum_{k}^{m}\mathbf{d}_k * \mathbf{z}_k\right\|_2^2 + \lambda\|\mathbf{s}\|_1 + \frac{\nu}{2}\|\mathbf{F_u x}-\mathbf{y}\|_2^2$$

$$\frac{\rho}{2}\|\mathbf{z}-\mathbf{s}+\mathbf{u}\|_2^2 + \frac{\delta}{2}\|\mathbf{d}-\mathbf{g}+\mathbf{h}\|_2^2 \quad s.t. \quad \mathbf{g} = Proj(\mathbf{d}), \|\mathbf{g}\|_2^2 \leq 1 \tag{11}$$

where **d** and **g** are related by a projection operator to make **g** matches the image size, because they have used an element wise multiplication operation in Fourier domain instead of convolutional operation in image domain. Also, **u** and **h** are ADMM dual variables, whereas ρ and δ are regularization parameters.

It is obviously seen from equation (11) that, improper setting of the above five regularization parameters ($\tau, \lambda, \nu, \rho,$ and δ) may degrade the quality of the reconstructed image, especially that these parameters are application dependent. In order to solve this issue, we propose a novel algorithm in chapter 4, that relies on CSC model dispensing with ADMM algorithm and its irritating regularization parameters.

CHAPTER 3

THE PROPOSED K-SPACE TRAJECTORY

In this chapter, we are discussing the proposed MRI undersampling technique that solve the incoherence problem of the traditional Cartesian leveraging its simple procedure.

3.2 The Procedure

The procedure of getting axial view of undersampled MRI brain image using Cartesian trajectory is shown in Figure 9. Depending on the desired view of the image, single gradient will operate as G_{PE} for the whole process to get two-dimensional image, allowing for one-dimensional incoherent subsampling. This can be done by randomly choosing certain values of G_{PE} to be sampled. Enjoying the same simplicity, the proposed trajectory applies two different Cartesian trajectories in perpendicular manner, permitting for two-dimensional incoherent subsampling. Firstly, part of the desired data is detected using traditional Cartesian trajectory in horizontal fashion by making G_x and G_y to operate as G_{FE} and G_{PE} respectively. Later, the roles of G_x and G_y are flipped, which will allow to detect the remaining K-space data in a vertical fashion. Finally, the resultant data of these two steps are merged to form the resultant undersampled K-space data. This procedure produces redundant K-space data as samples to be at the intersection of horizontal and vertical trajectories are detected twice. So, we use the average of the two values while forming the K-space data. Figure 10 summarizes the process of using the proposed trajectory to undersample the K-space data of brain axial view image.

Instead of sampling the K-space data in a fully random fashion, we employ pseudo-random sampling. In this approach, a fraction of the detected rows and columns come from the center of K-space, while the rest are selected randomly across the K-space. In particular, 20% of the rows and columns are detected from the center of K-space as it has been shown to achieve better PSNR of the reconstructed MRI image [6].

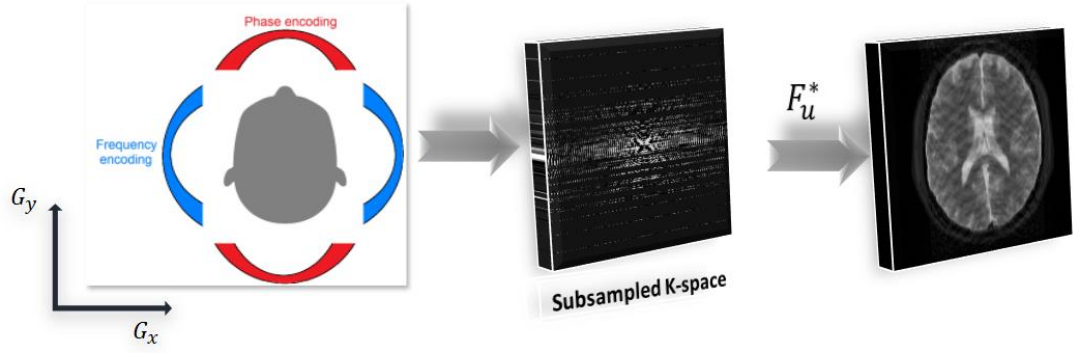

Figure 9 Cartesian trajectory configuration for detecting brain axial view image.

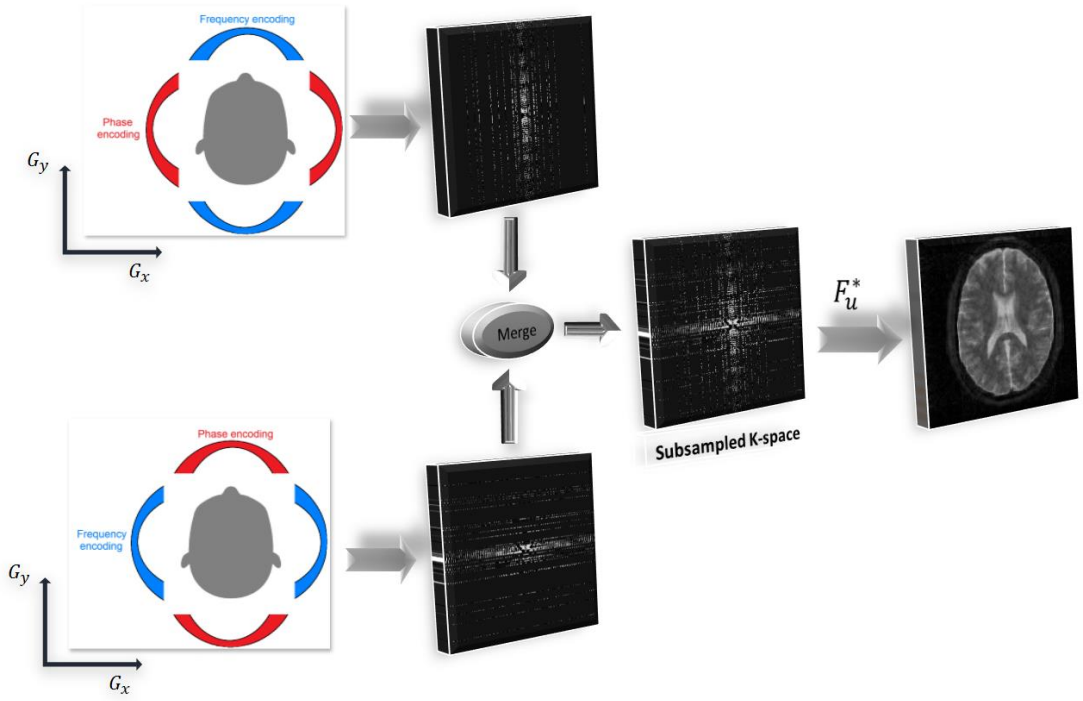

Figure 10 Proposed trajectory configuration for detecting brain axial view image.

3.2 MRI Sequences Using the Proposed Trajectory

The MRI sequences of traditional Cartesian trajectory can be applied for the proposed trajectory after slight modification. This is possible due to the similarity in the executional procedure of the two trajectories. In Figure 11, we show the implementation of Fast Spin Echo sequence (FSE) with only two excitations on both trajectories. The only difference between the two methods appears in the function of G_y and G_x. This simple procedure elegantly solves the problem of improving the scanned image quality with additional requirements on computations and MRI hardware.

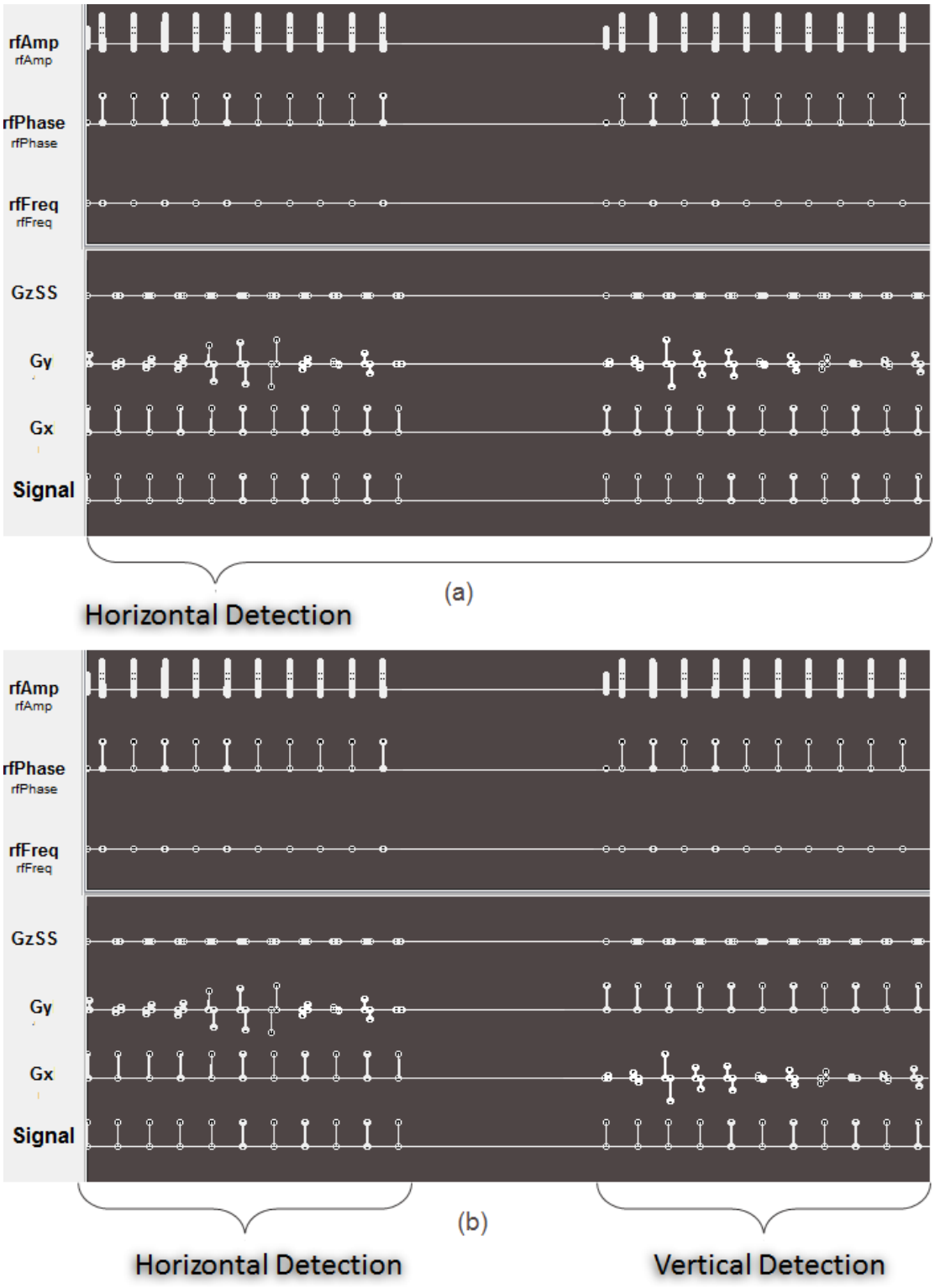

Figure 11 Implementation of FSE sequence on (a) traditional Cartesian trajectory. (b) proposed trajectory. The values of GPE are randomized to select the sample rows incoherently in both trajectories.

3.3 Point Spread Function (PSF)

I compare the incoherency of the proposed trajectory (Perpendicular trajectory) with that of the traditional Cartesian. To do so, we calculate the reconstructed PSF using the corresponding masks for the Cartesian and the proposed trajectories as shown in Figures 12(b) and 12(d), respectively. The PSF corresponding to the proposed trajectory exhibits lower sidelobes as compared to that of the traditional Cartesian. The height of the sidelobes indicate the intensity of aliasing artefacts produced by the undersampling process. This shows that the proposed trajectory results in higher incoherency of sampled data. This is also supported by the calculation of the peak sidelobe ratio (PSLR) [17] of the reconstructed PSFs, which were around -8.633 dB and -7.242 dB for the proposed and the traditional Cartesian trajectories, respectively, at 4.2 undersampling factor. PSLR is defined as follow:

$$\text{PSLR} = 10 \log_{10} \frac{I_s}{I_m} \tag{12}$$

where I_s stands for the peak level of the most intense sidelobe, and I_m stands for the peak level of the main-lobe.

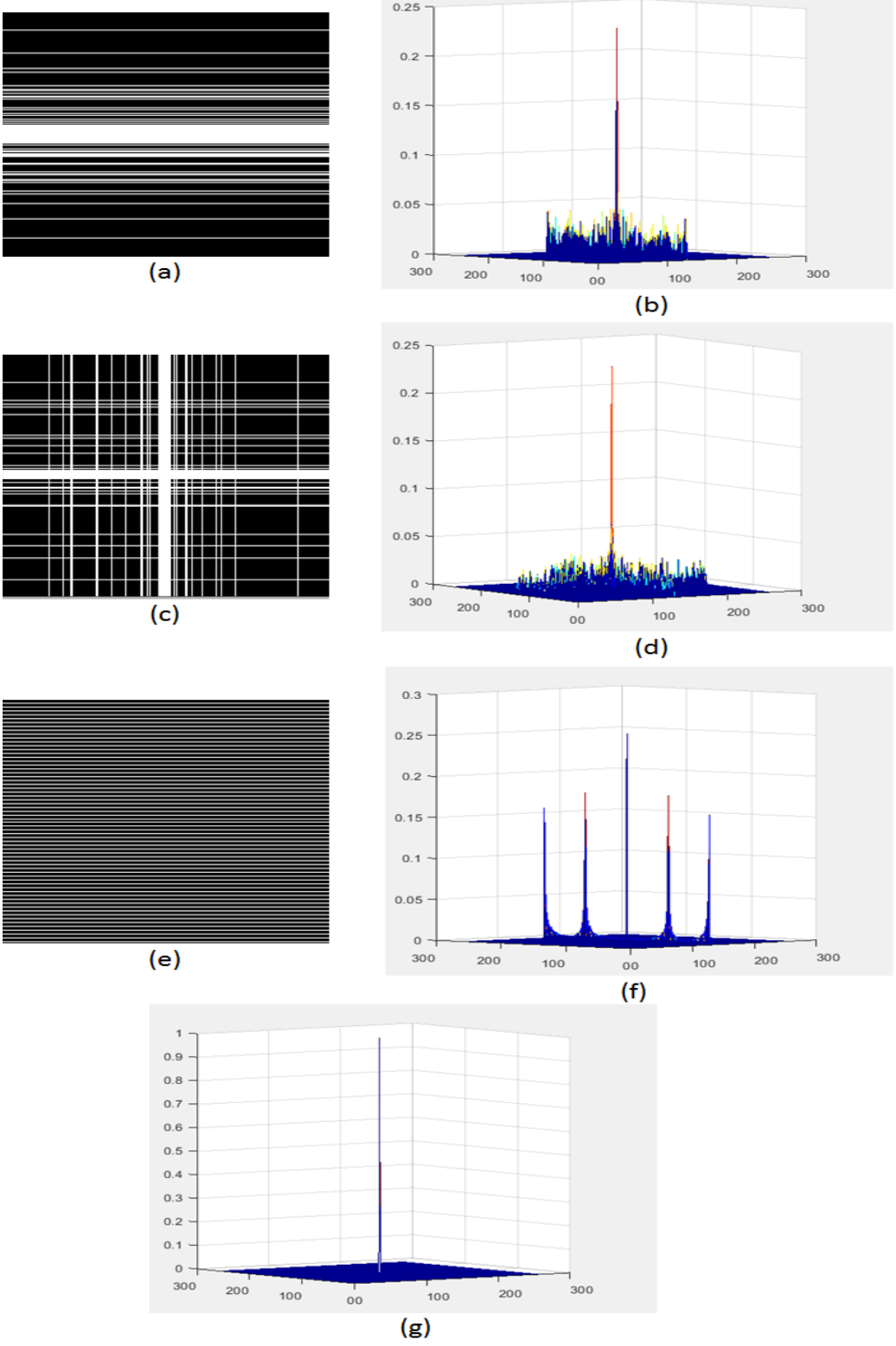

Figure 12 Masks of the proposed and Cartesian trajectories along with the reconstructed PSFs. Sampled rows are shown in white. The white bands in the middle of each mask are due to pseudo-random sampling. (a) Cartesian trajectory mask. (b) reconstructed PSF using (a). (c) Proposed trajectory mask. (d) reconstructed PSF using (c). (e) 4-folded Uniform undersampling mask. (f) reconstructed PSF using (e). (g) Original PSF.

3.4 Experiment and Results

To qualify the effectiveness of the proposed trajectory, we compare its performance with that of traditional Cartesian trajectory. We implement both trajectories to generate undersampled K-space data of brain axial view image using MRiLab simulation toolbox [28]. Gradient Echo (GE) and FSE sequences have been used to generate T1 and T2 weighted images, respectively. The parameters that have been used to generate the images are described in the next subsection.

3.4.1 Simulation Setup

I have used fixed slice thickness of 6mm and flip angle value equal to 90^{o}. In FSE sequence, we have set the ratio of repetition time over the Echo time (TR/TE) equal to 10000/70ms, while for GE sequence, we have set it to 10000/50ms.

In this experiment, we have tested our method using six different undersampling factors applied on a fully-sampled image of dimension 256×256. The chosen values of the undersampling factor are controlled by the Echo Train Length (ETL) and the number of spoke parameters used in FSE. Taking into consideration the nature of the proposed trajectory, we choose the number of spokes in FSE to be an even number, such that, it is equally separable into vertical and horizontal spokes. Therefore, we set the number of spokes used in GE to be harmonious to the undersampling factors that calculated for FSE. The details of these parameters are provided in Table 1.

Table 1 Details of the simulation parameters for both FSE and GE sequences and its corresponding undersampling factors.

FSE		**GE**	**Undersampling**
Spokes Number	ETL	Spokes Number	**Factor**
8	21	170	**1.5**
6	16	98	**2.6**
4	19	76	**3.4**
4	15	60	**4.2**
4	12	48	**5.4**
2	19	38	**6.8**

3.4.2 The Reconstruction Approach

I use MRiLab toolbox to generate K-space data according to the configurations mentioned above. After getting the undersampled K-space matrices with different MRI imaging types and undersampling factors, we reconstruct the corresponding images using FDLCP algorithm [29]. FDLCP is one of the most recent and successful CS reconstruction algorithms based on patch-based dictionary learning approach. The MATLAB code of this algorithm is available online [30] and has been used in this research work to test the proposed undersampling approach.

3.4.3 Results

The simulation results of the undersampled T1 and T2 weighted brain images are shown in Figure 13 and Figure 14, respectively. The image on the top-left side of Figure. 13 is the reconstructed brain image from a fully sampled K-space (according to the Nyquist

criterion). This image is formed by applying the inverse Fourier transform. The rest of the images in the first row from left to right (i.e. Figure 13 (b, c, d)) are also reconstructed using inverse Fourier transform when the K-space was undersampled by a factor of 4.2 using the traditional Cartesian, the proposed, and the radial trajectories. In order to construct images using the radial trajectory, we apply a radial mask with golden angle undersampling technique [31] on the full sampled K-space. The reconstructed images using the FDLCP algorithm are shown in parts (e, f, g) of Figure 13. The error images shown in the figures illustrate the absolute difference between the reconstructed images and the corresponding full sampled one. Similarly, the results for T2 weighted brain image are shown in Figure 14. It is obvious from these figures, that, fine details of the brain MRI image have been recovered in a much better way in case of the proposed trajectory for both T1 and T2 image cases. However, the images suffer from irreversible ringing artefacts introduced in the reconstruction process when using the traditional Cartesian trajectory. The figures show a comparable performance between the proposed and radial trajectory. The only such difference is located outside the brain boundary (on the black background), which is insignificant.

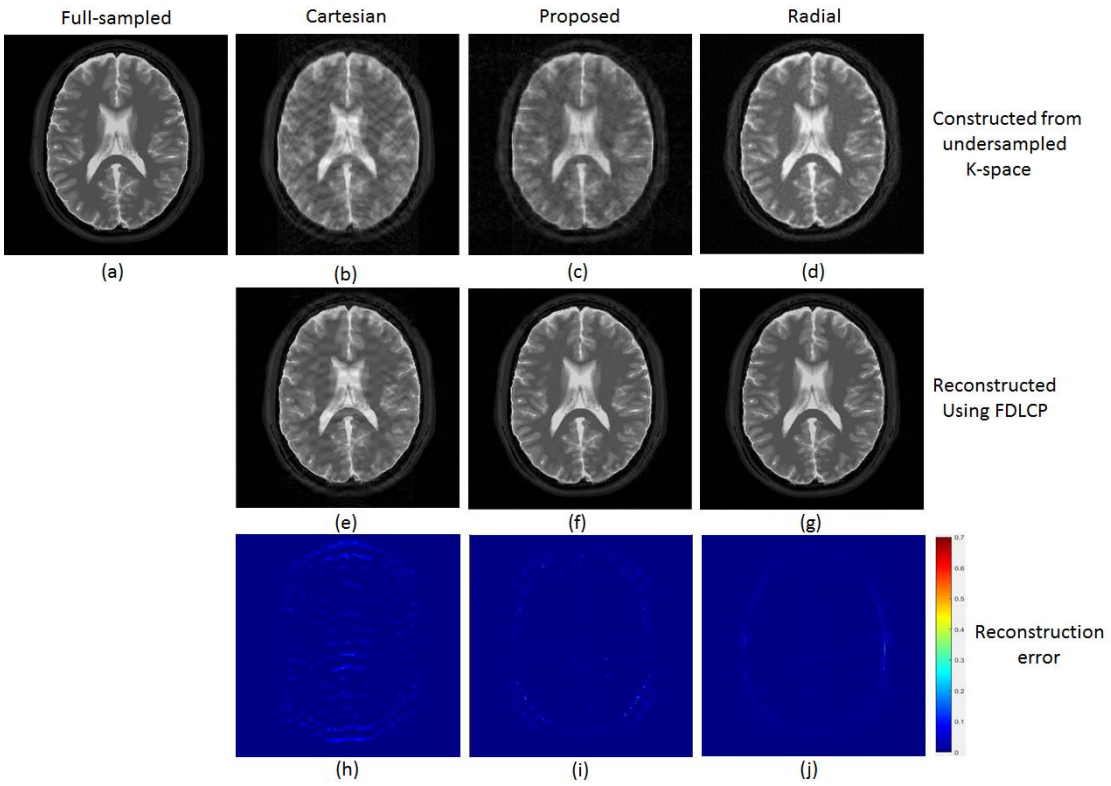

Figure 13 Reconstructed T1 weighted brain images and errors with 4.2 undersampling factor. (a) Full-sampled brain image. (b) Undersampled image using pseudo-random Cartesian trajectory. (c) Undersampled image using pseudo-random of the proposed trajectory. (d) Undersampled image using radial trajectory with golden angle undersampling method. (e)-(g) reconstructed images from (b)-(d). (h)-(j) reconstruction error magnitudes of (e)-(g).

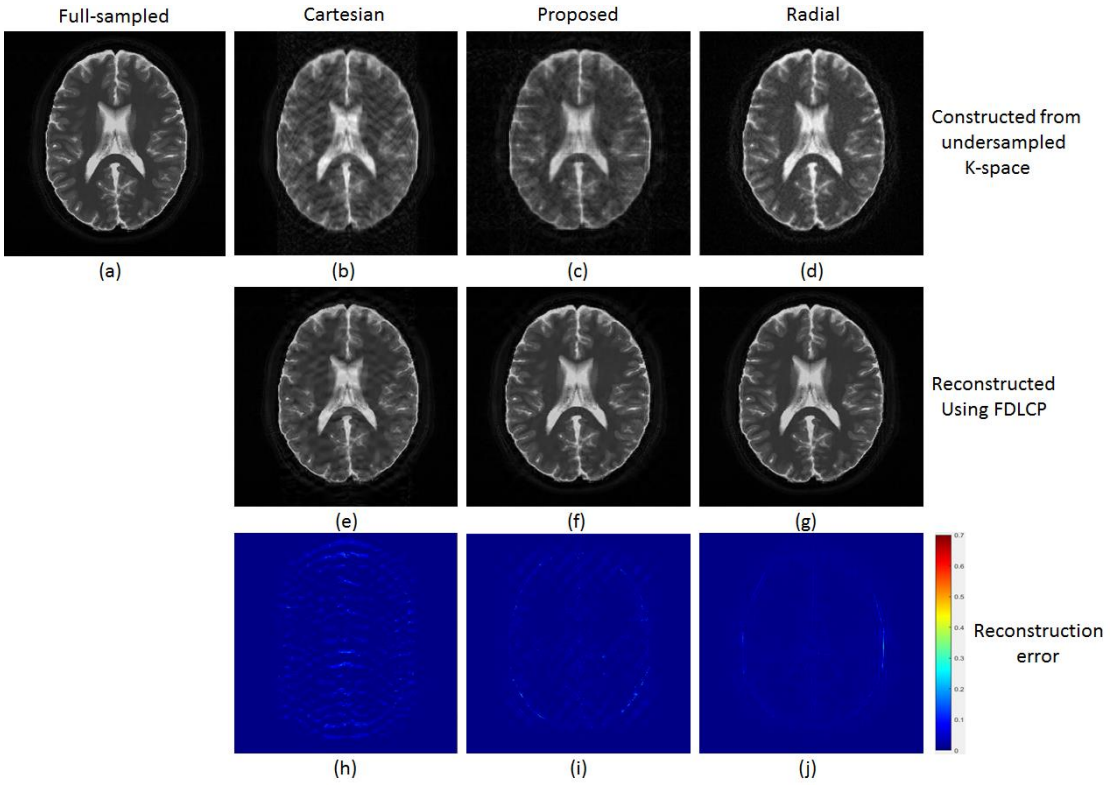

Figure 14 Reconstructed T2 weighted brain images and errors with 4.2 undersampling factor. (a) Full-sampled brain image. (b) Undersampled image using pseudo-random Cartesian trajectory. (c) Undersampled image using pseudo-random of the proposed trajectory. (d) Undersampled image using radial trajectory with golden angle undersampling method. (e)-(g) reconstructed images from (b)-(d). (h)-(j) reconstruction error magnitudes of (e)-(g).

To make a full comparison, we calculate the relative l_2 norm error RLNE [22] for the six different undersampling factors for both T1 and T2 weighted images.

$$\text{RLNE} = \|\mathbf{x}^* - \mathbf{x}\|_2 / \|\mathbf{x}\|_2 \tag{13}$$

where $\mathbf{x}^*$ is the reconstructed image and $\mathbf{x}$ is the reference full-sampled image. The results for both T1 and T2 cases are shown in Figure 15 (a) and (b). The results show that as the undersampled factor increases, the performance of both Cartesian and the proposed trajectory decrease. However, the degradation performance of the proposed trajectory is much less as compared to the traditional Cartesian. This reinforces our claim that the proposed trajectory is better than the traditional Cartesian.

The lower performance of the proposed trajectory for smaller undersampling factors is due to the redundancy in K-space sampling as discussed in section 3.1. This drawback is not significant as usually higher values of undersampled factor are used as evident from the literature [12, 14, 29].

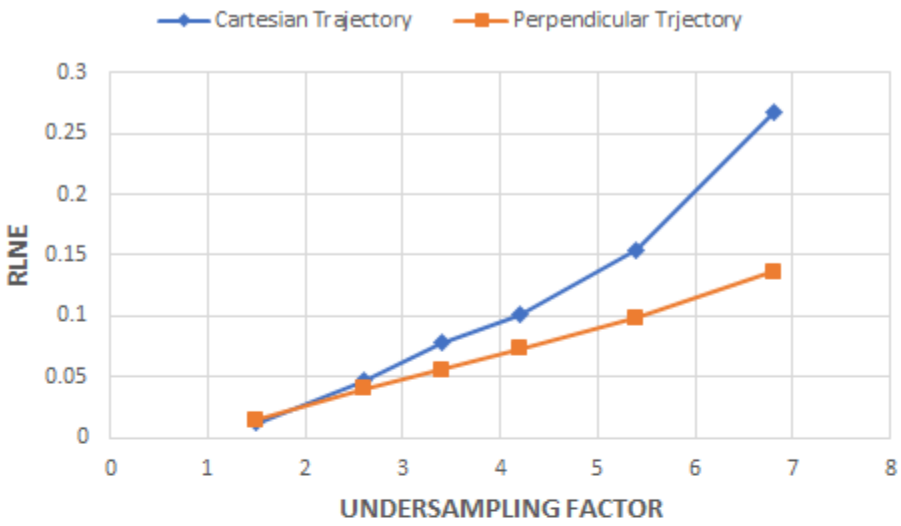

(a)

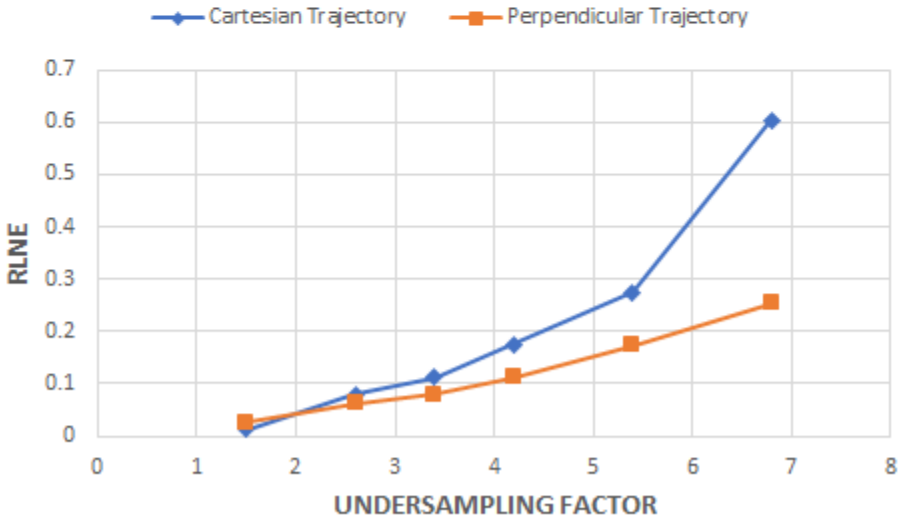

(b)

Figure 15 RLNE of the reconstructed brain images versus the undersampling factor. (a) for T1 weighted images. (b) for T2 weighted images.

3.5 Summary

In this chapter, an efficient MRI-CS undersampling technique leveraging the executional simplicity of the conventional Cartesian trajectory is proposed. This technique permits higher level of subsampling incoherence such that, it improves the image reconstruction process. This improvement helps to dramatically increase the undersampling factor used in future MRI compressed sensing techniques in order to decrease the scanning time with better reconstruction results.

CHAPTER 4

THE PROPOSED RECONSTRUCTION ALGORITHM

In this chapter, we are proposing a higher performance CSC-based algorithm to reconstruct highly undersampled MRI images, leveraging the LoBCoD algorithm instead of relying on ADMM and its disturbing regularization parameters.

4.1 The Algorithm

Zisselman et al. [15] have reformulated the CSC structure into matrix vector product, as follows:

$$\min_{\mathbf{D},\boldsymbol{\Gamma}} \frac{1}{2}\|\mathbf{x}-\mathbf{D}\boldsymbol{\Gamma}\|_2^2+\lambda\|\boldsymbol{\Gamma}\|_1 \tag{14}$$

where $\mathbf{D}$ is the global dictionary matrix composite of shifted version of local dictionary $\mathbf{D}_L$ of size $n \times m$, and $\boldsymbol{\Gamma}$ is the global sparse vector present the feature maps $\{\mathbf{z}_k\}_{k=1}^m$ in an interlaced concatenation vector form (see [32] for more details).

In this section, we want to reconstruct MRI images from undersampled K-space data, therefore, leveraging the data consistency part added in equation (9) after learning dictionary process, we modified the general equation into the following:

$$\min_{\mathbf{x},\mathbf{D},\boldsymbol{\Gamma}} \frac{1}{2}\|\mathbf{x}-\mathbf{D}\boldsymbol{\Gamma}\|_2^2+\lambda\|\boldsymbol{\Gamma}\|_1+\frac{\nu}{2}\|\mathbf{F_u}\mathbf{x}-\mathbf{y}\|_2^2 \tag{15}$$

Making our algorithm consists three main steps: 1) sparse feature maps calculation. 2) dictionary learning. 3) updating the reconstructed image with the help of the data consistency part ($\frac{\nu}{2}\|\mathbf{F_u}\mathbf{x}-\mathbf{y}\|_2^2$). Which it has been summarized in Figure 16.

1) Sparse Feature Maps calculation step:

Due to the inapplicability of solving equation (14) in a global manner (because of the huge dimensionality of $\mathbf{D}$ and $\mathbf{\Gamma}$), we leverage the model proposed in [32] by splitting the global sparse vector into N^2 non-overlapping of m dimensional local sparse needles $\boldsymbol{\alpha}_i$. By this, the reconstructed vectorized image ($\mathbf{x}$) can be presented as $\mathbf{x} = \sum_{i=1}^{N^2} \mathbf{P}_i^T \mathbf{D}_L \boldsymbol{\alpha}_i$,where $\mathbf{P}_i^T \in R^{N^2 \times n}$ is an operator that localizes $\mathbf{D}_L \boldsymbol{\alpha}_i$ into the i-th position of a vector of length N^2, and pads the rest vector values by zeros. Which converts equation (14) into the following:

$$\min_{\boldsymbol{\alpha}_i} \frac{1}{2} \left\| \mathbf{x} - \sum_{i=1}^{N^2} \mathbf{P}_i^T \mathbf{D}_L \boldsymbol{\alpha}_i \right\|_2^2 + \lambda \sum_{i=1}^{N^2} \|\boldsymbol{\alpha}_i\|_1 \tag{16}$$

The main concept that LoBCoD algorithm has used to optimize the global vector $\mathbf{\Gamma}$, is to optimize each of its needle α_i one at a time, by reformulating equation (16) into:

$$\min_{\boldsymbol{\alpha}_i} \frac{1}{2} \left\| \left(\mathbf{x} - \sum_{\substack{j=1 \\ j \neq i}}^{N^2} \mathbf{P}_j^T \mathbf{D}_L \boldsymbol{\alpha}_j \right) - \mathbf{P}_i^T \mathbf{D}_L \boldsymbol{\alpha}_i \right\|_2^2 + \lambda \|\boldsymbol{\alpha}_i\|_1 \tag{17}$$

And by introducing the $\mathbf{R}_i = (\mathbf{x} - \sum_{\substack{j=1 \\ j \neq i}}^{N^2} \mathbf{P}_j \mathbf{D}_L \boldsymbol{\alpha}_i)$ to be the image residual without the i-th needle ($\boldsymbol{\alpha}_i$) contribution, equation (17) can be rewritten as:

$$\min_{\boldsymbol{\alpha}_i} \frac{1}{2} \left\| \mathbf{R}_i - \mathbf{P}_i^T \mathbf{D}_L \boldsymbol{\alpha}_i \right\|_2^2 + \lambda \|\boldsymbol{\alpha}_i\|_1 \tag{18}$$

Therefore, as follow:

$$\min_{\boldsymbol{\alpha}_i} \frac{1}{2} \|\mathbf{P}_i \mathbf{R}_i - \mathbf{D}_L \boldsymbol{\alpha}_i\|_2^2 + \lambda \|\boldsymbol{\alpha}_i\|_1 \tag{19}$$

So, in order to do one step iteration to optimize the global $\mathbf{\Gamma}$ vector, N^2 sub-convex optimizations have to be operated for each α_i needle, such that:

$$\boldsymbol{\alpha}_i = \underset{\boldsymbol{\alpha}_i}{\operatorname{argmin}} \frac{1}{2} \|\mathbf{P}_i \mathbf{R}_i - \mathbf{D}_L \boldsymbol{\alpha}_i\|_2^2 + \lambda \|\boldsymbol{\alpha}_i\|_1$$

2) Dictionary Learning

After finding the sparse feature maps, the global dictionary matrix update is done by updating its local matrix $\mathbf{D}_L$. This is performed by solving the following minimization problem, subject to the constraint of normalized dictionary columns:

$$\min_{\mathbf{D}_L} \frac{1}{2} \left\| \mathbf{x} - \sum_{i=1}^{N^2} \mathbf{P}_i^T \mathbf{D}_L \boldsymbol{\alpha}_i \right\|_2^2 \qquad s.t. \|\{\mathbf{d}_i\}_{i=1}^m\|_2 = 1 \tag{20}$$

This can be achieved using projected steepest descent. The gradient of the quadratic term in equation (20) w.r.t. $\mathbf{D}_L$ is:

$$\nabla \mathbf{D}_L = -\sum_{i=1}^{N^2} \mathbf{P}_i (\mathbf{x} - \mathbf{x}^*). \boldsymbol{\alpha}_i^T \tag{21}$$

where $\mathbf{x}^*$ is the most recent reconstructed signal. The final update step for $\mathbf{D}_L$ is given as:

$$\mathbf{D}_L = \mathcal{P}[\mathbf{D}_L - \eta \nabla \mathbf{D}_L] \tag{22}$$

where η is a learning step size constant which we set it equal to 1.5% of the norm of the gradient as proposed in [33], and $\mathcal{P}[.]$ is a normalization operator that forces each atom ($\{\mathbf{d}_i\}_{i=1}^m$) to have unit norm.

Updating $\mathbf{D}_L$ after updating the whole global sparse vector $\mathbf{\Gamma}$ is inefficient and exhibits very slow convergence, especially, when N^2 is very large. Therefore, we used the idea of

stochastic gradient decent by computing the gradient of $\mathbf{D}_L$ after updating just a few numbers of sparse needles at a time.

So, a layer L_i has been defined that contains a set of needles $\boldsymbol{\alpha}_i$ such that they don't have an overlapping impact on the reconstructed image $\mathbf{x}^*$ nor the residual vector $\mathbf{R}$, therefore, we update the dictionary $\mathbf{D}_L$ after each layer step.

This allows to reduce the outer iteration for global sparse vector $\boldsymbol{\Gamma}$ calculation from N^2 number of needles (or iterations) to n number of layers (or iterations), which have $(2n-1)$ number of inner needles (or iterations). Therefore, it permits for further speeding up using parallel computing in every layer calculation step.

3) Reconstructed Image Updating

After dictionary learning convergence step and calculating the latest global sparse vector $\boldsymbol{\Gamma}$, we updated the reconstructed image such that it reserves some data consistency from the K-space acquired data ($\mathbf{y}$), by solving the quadratic terms of equation (15) as follow:

$$\mathbf{x} = \underset{\mathbf{x}}{\operatorname{argmin}} \frac{1}{2} \|\mathbf{x} - \mathbf{D}\boldsymbol{\Gamma}\|_2^2 + \frac{\nu}{2} \|\mathbf{F_u}\mathbf{x} - \mathbf{y}\|_2^2 \tag{23}$$

$$(1 + \nu \mathbf{F_u}^H \mathbf{F_u})\mathbf{x} = \mathbf{D}\boldsymbol{\Gamma} + \nu \mathbf{F_u}^H \mathbf{y} \tag{24}$$

where the superscript H is the Hermitian transpose operator, and $\mathbf{F_u}^H \mathbf{F_u}$ multiplication is nothing but the corresponding mask operator that caused K-space undersampling data. And after taking the Fourier transform for both sides, we get:

$$\mathbf{x}_f = (\mathbf{F}\mathbf{D}\boldsymbol{\Gamma} + \nu \mathbf{y})/(1 + \nu \mathbf{M}) \tag{25}$$

Where **M** is the mask matrix, and $\mathbf{x}_f$ is the Fourier transform of the reconstructed image. Which it can be restates as follows:

$$\mathbf{x}_f = \begin{cases} \mathbf{FD\Gamma} & , \ (k_x, k_y) \notin \Omega \\ \frac{\mathbf{FD\Gamma} + \nu \mathbf{y}}{1+\nu} & , \ (k_x, k_y) \in \Omega \end{cases} \tag{26}$$

where Ω refers to the K-space elements that have been sampled in the acquired data (**y**).This indicates that, the Fourier transform of the reconstructed image in unsampled K-space locations is nothing but the Fourier transform of the result gained from the dictionary learning and sparse vector calculation steps (**DΓ**), and it is equal to some sort of averaging operation with the acquired data (**y**) in sampled K-space locations, by assuming noisy cases ($\nu \neq \infty$).

ν regularized parameter explicitly presents the noise added in the measured K-space data while the data is in the observation process. In our model it is equal to (μ/σ), where, μ is a constant and σ is the standard deviation of the added noise by assuming independent and identically distributed (i.i.d) zero-mean complex Gaussian noise. Which increases the robustness of our algorithm in the present of noise.

Algorithm

Input: vectorized image ($\mathbf{x} = \mathbf{F}_{\mathbf{u}}^{H}\mathbf{y}$), initial dictionary $\mathbf{D}_L$, initial needles $\{\boldsymbol{\alpha}_i^0\}_{i=1}^{N^2}$

Output: Reconstructed MRI image $\mathbf{x}$

Initialization: $\mathbf{R} = \mathbf{x}$, $\mathbf{x}^* = 0$, $k = 0$

Main Iteration:

1) **While** *not converge* **do**

   $k = k + 1$

   For $j = 1{:}n$

   Computation of the Residual

   $$\mathbf{R}_j = \mathbf{R} + \sum_{i \in L_j} \mathbf{P}_i^T \mathbf{D}_L \boldsymbol{\alpha}_i$$

   Sparse calculation step: $\forall i \in L_j$ (in parallel)

   $$\boldsymbol{\alpha}_i^k = \underset{\boldsymbol{\alpha}_i}{\operatorname{argmin}} \frac{1}{2} \left\| \mathbf{P}_i \mathbf{R}_j - \mathbf{D}_L \boldsymbol{\alpha}_i \right\|_2^2 + \lambda \|\boldsymbol{\alpha}_i\|_1$$

   Updating $\mathbf{x}^*$:

   $$\mathbf{x}^* = \mathbf{x}^* + \sum_{i \in L_j} \mathbf{P}_i^T \mathbf{D}_L (\boldsymbol{\alpha}_i^k - \boldsymbol{\alpha}_i^{k-1})$$

   Computation of the residual:

   $$\mathbf{R} = \mathbf{x} - \mathbf{x}^*$$

   Computation of the $\mathbf{D}_L$ gradient:

   $$\nabla \mathbf{D}_L = -\sum_{i \in L_j} \mathbf{P}_i \mathbf{R}. \left(\boldsymbol{\alpha}_i^k\right)^T$$

   Stochastically dictionary updating:

   $$\mathbf{D}_L = \mathcal{P}[\mathbf{D}_L - \eta \nabla \mathbf{D}_L]$$

   End

   End

2) **Reference image updating** according to equation (26)

   $$\mathbf{x} = iFFT2(\mathbf{x}_f)$$

Figure 16 The proposed algorithm summary for undersampled MRI image reconstruction.

4.2 Parameters and Initializations

By overcoming the ADMM choosing multi-parameter issue as in [14], our algorithm consists of only two regularization parameters as seen in equation (15), λ which controls the sparsity of the sparse vector $\mathbf{\Gamma}$, and ν controls the data consistency of the reconstructed image, which simplify the reconstruction procedure and give better image quality in resultant. Moreover, the authors in [15] proposed an initialization for sparse vector needles that provide better approximation for input image by equally spreading the contribution to all sparse needles, which leads for faster convergence process, and yet better reconstruction quality, as shown in the following:

$$\boldsymbol{\alpha}_i^0 = \underset{\boldsymbol{\alpha}_i}{\operatorname{argmin}} \frac{1}{2} \left\| \frac{1}{n} \mathbf{P}_i \mathbf{x} - \mathbf{D}_L \boldsymbol{\alpha}_i \right\|_2^2 + \lambda \|\boldsymbol{\alpha}\|_1 \tag{27}$$

likewise, we use it in the initialization step of our proposed algorithm.

4.3 Results

In this section, the performance of the proposed algorithm is assessed at multiple undersampling factors, with and without noise. The images used in this experiment represent brain and spinal cord images. The subsampling scheme used is the Cartesian with random phase gradient values, as it is the most popular in real MRI scanner. Similarly to prior work on CSMRI [12, 22, 34, 35, 36], the CS data acquisition was simulated by subsampling the 2D discrete Fourier transform of the MR images (except in Figure. 21 where synthetic data is used, which has been extracted via MRiLab toolbox [29]). Our reconstruction method is compared with the state-of-the-art patch-based dictionary learning CSMRI (as denoted by DLMRI [12]) and the leading CSMRI method proposed

by Lustig et al. [22] with fixed wavelet and total variation dictionary, and the baseline zero-filling reconstruction. we have used one hundred kernels of size 11×11 in all our image cases. Figure 17 visualizes the kernel atoms using the proposed method and the state-of-the-art DLMRI, respectively. Our learning method can generate atoms that capture details of the image features much better than the patch-based learning method. Because the patch-based learning method generate smoother atoms (e.g., Gabor-like edges), its reconstruction process relies more on accurate sparse coding, which results in less-optimal convergence in the minimization process and higher error rates compared to our method.

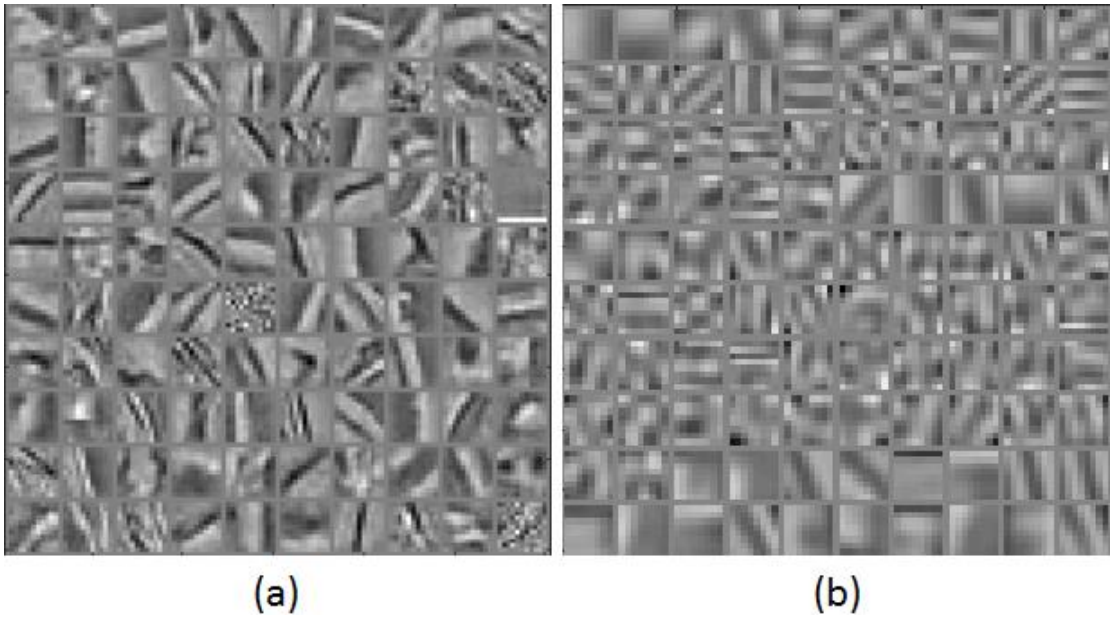

Figure 17 The learned kernels using (a) proposed method (b) DLMRI.

Along with the PSNR assessment calculation, Reconstruction performance is quantified by the RLNE.

4.3.1 Noiseless Case

The noiseless cases can be solved by performing a direct frequency fill-in at the reconstruction update step of our algorithm (see equation 29). we study the noiseless

scenario first in order to see the best, or ideal performance that can be obtained with our formulation and algorithm. Figure 18 shows the performance of the algorithm on a T2-weighted spinal image in sagittal view employing 1D incoherent Cartesian subsampling of k-space using four undersampling factor. The zero-filled Fourier reconstruction has significant undesirable ringing artefacts due to aliasing. Wavelet/TV based and the DLMRI are unable to remove the aliasing well, as obviously seen in the absolute error images. Some of the ringing artefacts in the zero-filled reconstruction persist in [22] more than the DLMRI result. In contrast, the result with the CSC based proposed method is seen to be free from ringing artefacts and close to perfect reconstruction. Figure 19(a) corresponds to the RLNE calculation using different undersampling factor and algorithms. Also it emphasizes the superiority of our reconstruction algorithm compare to DLMRI and the Wavelet/TV dictionary based algorithms in noiseless cases.

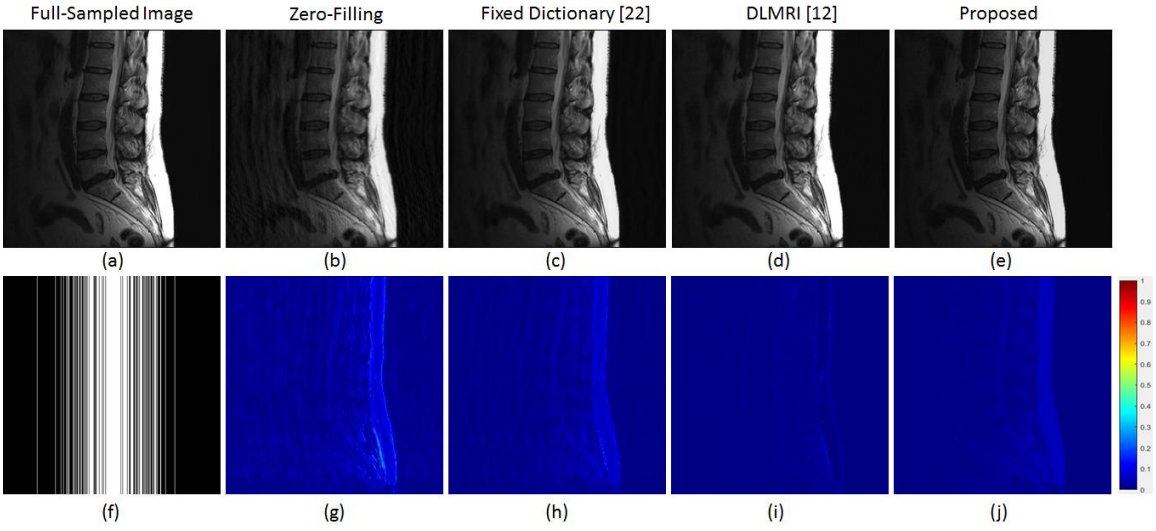

Figure 18 Reconstructed noise-free spinal images and errors using Cartesian subsampling with 4 undersampling factor. (a) Full-sampled image (b)–(e) reconstructed images based on zero-filling, Wavelet/TV based [3], DLMRI, and proposed, respectively, (f) Cartesian undersampling mask, (g)–(j) the absolute of reconstruction error corresponding to the above reconstructions.

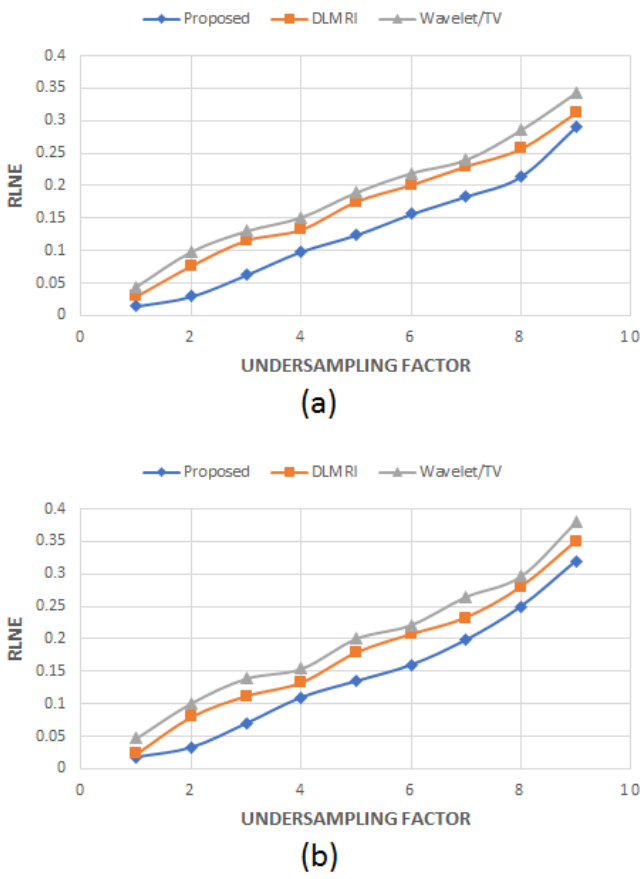

Figure 19 RLNE values versus different undersampling factors on (a) noise-free image ap-pear in Figure 18 (b) noisy image appear in Figure 20.

4.3.2 Noisy Case

The noisy case involves weighted averaging in k-space during the reconstruction update step of the proposed algorithm, as discussed in equation (26). Figure 20 describes the performance of our algorithm on a sagittal view T1-weighted brain image using cartesian subsampling at 4 undersampling factor. Zero-mean complex white Gaussian noise of standard deviation, $\sigma = 20$ was added to its k-space. The fully sampled noiseless image is shown along with the magnitude of the added-noise image in part (a) and (f) of the figure, respectively. The PSNR of the noisy image with respect to the reference is about 30.68 dB. The reconstruction using fixed Wavelet/TV dictionary algorithm is unable to sufficiently remove the aliasing and noise seen in the zero-filled result. However, DLMRI perform

better than [22] but with some large error appear near the cortex area of the brain image. Our algorithm, on the other hand provides a good reconstruction. The magnitude image of the reconstruction error for proposed algorithm shows pixel errors of much smaller magnitude and absence of ringing artefact as compared to that of DLMRI and Wavelet/TV algorithm based. The PSNR of the proposed result (with respect to the noise-free reference) is about 2.2 dB higher than that of DLMRI and 6.5 dB than that of fixed Wavelet/TV algorithm. It is also higher than the PSNR of both the fully sampled noisy image and the zero-filled result indicating good denoising and aliasing removal, which summarizes in Table 2. However, different undersampling factor has been assessed in Figure 19(b) shows better performance of the proposed method compared to the DLMRI and the Wavelet/TV based algorithm using RLNE index value.

Table 2 PSNR values of different reconstructions based on the noisy case appear in Figure 20.

	Noisy Full-Sampled	**Zero-Filled**	**Wavelet/TV**	**DLMRI**	**Proposed**
PSNR	30.68	22.42	27.18	31.48	33.68

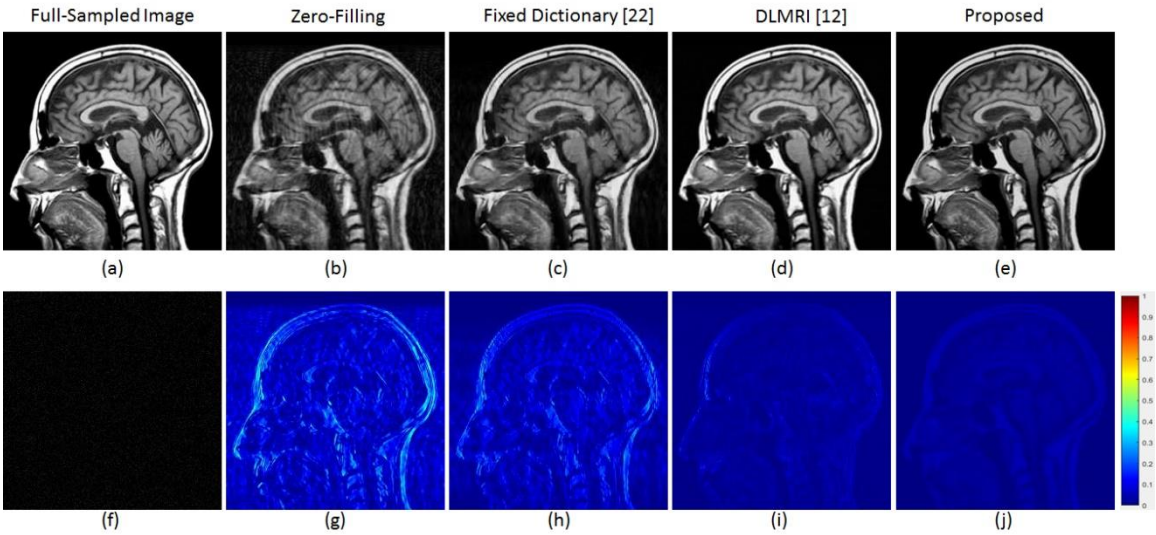

Figure 20 Reconstructed noisy sagittal view brain images and errors using Cartesian sub-sampling with 4 undersampling factor. (a) Full-sampled noise-free image (b)–(e) reconstructed images based on zero-filling, Wavelet/TV based [3], DLMRI, and proposed, , respectively, (f) noise magnitude added to (a), (g)–(j) the absolute of re-construction error corresponding to the above reconstructions.

4.3.3 Synthetic Case

In this section, we have generated a T2 weighted brain image data using MRiLab tool box. Figure 21 shows the corresponding data reconstruction using zero-filling, Wavelet/TV based algorithm, DLMRI, and proposed method respectively. The fully sampled brain data is acquired using a Fast Spin Echo (FSE) sequence of matrix size = 256 × 256, TR/TE= 10000/70ms, field of view = 24 × 20 cm^2, slice thickness = 6mm, flip angle = 90º, echo train length = 16 with 16 excitations. Part (b) of the figure shows the zero-filled image with undersampling factor of 3.4 using echo train length = 19 with 4 excitations. As it can be obviously seen, Wavelet/TV based algorithm introduces obvious ghost like artefacts whereas DLMRI causes ringing artefact concentrated more around the edges. However, the proposed CSC based algorithm reconstructs the image best in Figure 21(e) and leads to minimal loss of image features in Figure 21(i). The quality values listed in Table 3

demonstrates that the proposed algorithm enjoys the lowest RLNE and highest PSNR among all methods for this synthetic experiment.

Table 3 PSNR and RLNE values of different reconstructions based on the synthetic axial view brain image appear in Figure 21.

	Zero-Filled	Wavelet/TV	DLMRI	Proposed
PSNR	24.9736	28.2208	28.5654	34.9923
RLNE	0.2366	0.1628	0.1565	0.0747

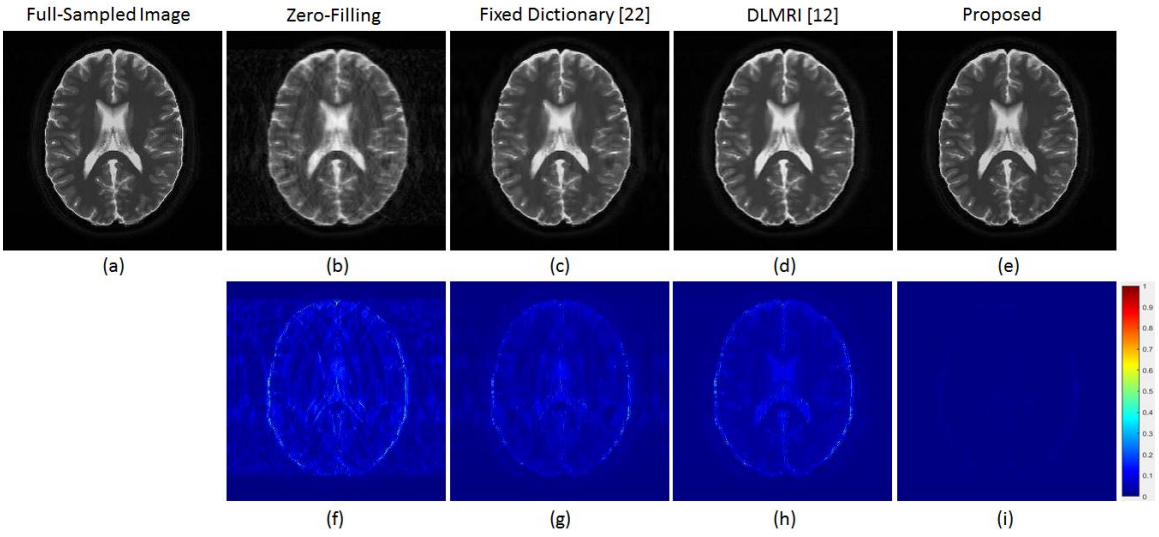

Figure 21 Reconstructed synthetic axial view brain image and errors using MRiLab toolbox with 3.4 undersampling factor. (a) Full-sampled image (b)–(e) reconstructed im-ages based on zero-filling, Wavelet/TV based [22], DLMRI, and proposed, respec-tively, (f)–(i) the absolute of reconstruction error corresponding to the above re-constructions.

4.4 Summary

In this chapter, a novel CSC-based algorithm for MR image reconstruction has been proposed. The proposed method overcomes the many ADMM tuning parameters proposed

in [14] Leveraging the LoBCoD algorithm. It has the ability of detection image features in a better way than that of the state-of-the-art patch-based dictionary learning method, which yields in higher reconstruction accuracy. A variety of experimental results demonstrated the superior performance of the method under various undersampling factors. It provided superior performance in both noiseless and noisy cases.

CHAPTER 5

CONCLUSIONS AND FUTURE WORK

In this thesis, we have treated one of the most problematic issue in MRI CS, which is the incoherence subsampling. We propose a simple and elegant method of subsampling MRI data that can be easily incorporated in real MRI machines. This is significant because it improves the image construction speed without compromising image quality. Further, the method does not need any additional hardware and computational requirements when compared with traditional method (Cartesian trajectory).

Also, we have introduced a non-linear MRI CS reconstruction algorithm based on contemporary sparse coding model (CSC). This solves two main and fundamental drawbacks of the most recently used algorithms, which is presented by: 1) using ADMM algorithm with many disturbing regularization parameters, 2) relying on patch-based techniques, therefore, losing most of global image feature during the reconstruction process.

In conclusion, the solutions have been offered in this research work permits for further acceleration in MRI imaging procedure without resulting in image degradation. As a result, it will improve the quality of MRI imaging technique because it will allow faster scans for patients who are anxious and cannot keep still.

We have tested the proposed trajectory using MRiLab simulation toolbox considering static MRI application with T2 and T1 weighed brain images. That makes the verification of its applicability on dynamic MRI applications using real scanner is our future work.

References

[1] D. C. Peters, J. A. Derbyshire, and E. R. Mcveigh, "Centering the projection reconstruction trajectory: Reducing gradient delay errors," *Magnetic Resonance in Medicine*, vol. 50, no. 1, pp. 1–6, 2003.

[2] K. T. Block, H. Chandarana, G. Fatterpekar, M. Hagiwara, S. Milla, T. Mulholland, M. Bruno, C. Geppert, and D. K. Sodickson, "Improving the robustness of clinical T1-weighted MRI using radial VIBE", *Clin Head-to-toe Imaging* Vol. 5, pp. 6–11, 2013.

[3] M. Lustig, D. Donoho, J. Santos, and J. Pauly, "Compressed Sensing MRI," *IEEE Signal Processing Magazine*, vol. 25, no. 2, pp. 72–82, 2008.

[4] D. Donoho, "Compressed sensing," *IEEE Transactions on Information Theory*, vol. 52, no. 4, pp. 1289–1306, 2006.

[5] E. Candes and M. Wakin, "An Introduction To Compressive Sampling," *IEEE Signal Processing Magazine*, vol. 25, no. 2, pp. 21–30, 2008.

[6] D.-D. Liu, D. Liang, X. Liu, and Y.-T. Zhang, "Under-sampling trajectory design for compressed sensing MRI," *2012 Annual International Conference of the IEEE Engineering in Medicine and Biology Society*, 2012.

[7] E. S. Ilievska and Z. A. Ivanovski, "Customized k-space trajectory for compressed sensing MRI," *2011 19thTelecommunications Forum (TELFOR) Proceedings of Papers*, 2011.

[8] S. Geethanath, R. Reddy, A. S. Konar, S. Imam, R. Sundaresan, R. B. D. R., and R. Venkatesan, "Compressed Sensing MRI: A Review," *Critical Reviews in Biomedical Engineering*, vol. 41, no. 3, pp. 183–204, 2013.

[9] S. Sharma and K. V. S. Hari, "Four-shot non-cartesian trajectories for k-space sampling in MRI," *CSI Transactions on ICT*, vol. 6, no. 1, pp. 11–16, 2017.

[10] R. K. Robison, Z. Li, D. Wang, M. B. Ooi, and J. G. Pipe, "Correction of B0 eddy current effects in spiral MRI," *Magnetic Resonance in Medicine*, vol. 81, no. 4, pp. 2501–2513, 2018.

[11] J. Liu, and D. Saloner, "Accelerated MRI with CIRcular Cartesian UnderSampling (CIRCUS): a variable density Cartesian sampling strategy for compressed sensing and parallel imaging", *Quant Imaging Med Surg*, vol. 4, no. 1, pp. 57-67, 2014.

[12] S. Ravishankar and Y. Bresler, “MR Image Reconstruction From Highly Undersampled k-Space Data by Dictionary Learning,” *IEEE Transactions on Medical Imaging*, vol. 30, no. 5, pp. 1028–1041, 2011.

[13] S. Boyd, “Distributed Optimization and Statistical Learning via the Alternating Direction Method of Multipliers,” *Foundations and Trends® in Machine Learning*, vol. 3, no. 1, pp. 1–122, 2010.

[14] T. M. Quan and W.-K. Jeong, “Compressed sensing reconstruction of dynamic contrast enhanced MRI using GPU-accelerated convolutional sparse coding,” *2016 IEEE 13th International Symposium on Biomedical Imaging (ISBI)*, 2016.

[15] Ev Zisselman, J. Sulamy and M. Elad, "A Local Block Coordinate Descent Algorithm for the Convolutional Sparse Coding Model" [online] Available: https://arxiv.org/abs/1811.00312.

[16] The Physics of Magnetic Resonance Imaging, accessed 3 January 2019, http://www.schoolphysics.co.uk/age16-19/Atomic%20physics/Atomic%20structure%20and%20ions/text/MRI/index.html.

[17] Slice Selection, accessed 3 January 2019, http://www.mrishark.com/slice-selection.html.

[18] Gradient echo sequence, accessed 3 January 2019, https://www.researchgate.net/figure/Pulse-diagram-of-a-gradient-echo-sequence_fig1_6442524.

[19] Fast Spin Echo, accessed 3 January 2019, http://xrayphysics.com/sequences.html.

[20] Different types of K-space trajectories in MRI, accessed 3 January 2019, https://mediri.com/en/medical-imaging-research.

[21] MRI K-space, accessed 3 January 2019, https://www.cambridge.org/core/books/introduction-to-functional-magnetic-resonance-imaging/principles-of-magnetic-resonance-imaging/21E65E09696182D6D7E265CFAC75B881/core-reader.

[22] M. Lustig, D. Donoho, and J. M. Pauly, “Sparse MRI: The application of compressed sensing for rapid MR imaging,” *Magnetic Resonance in Medicine*, vol. 58, no. 6, pp. 1182–1195, 2007.

[23] W. Hao, X. Qu, Z. Dong, and J. Li, “Fast iterative contourlet thresholding for compressed sensing MRI,” *Electronics Letters*, vol. 49, no. 19, pp. 1206–1208, 2013.

[24] M. Aharon, M. Elad, and A. Bruckstein, “K-SVD: An Algorithm for Designing Overcomplete Dictionaries for Sparse Representation,” *IEEE Transactions on Signal Processing*, vol. 54, no. 11, pp. 4311–4322, 2006.

[25] H. Bristow, A. Eriksson, and S. Lucey, “Fast Convolutional Sparse Coding,” *2013 IEEE Conference on Computer Vision and Pattern Recognition*, 2013.

[26] H. Bristow and S. Lucey, “Optimization methods for convolutional sparse coding,” arXiv:1406.2407, 2014.

[27] B. Kong and C. C. Fowlkes. (2014). “Fast convolutional sparse coding (FCSC) ” Dept. Comput. Sci. Univ. California Irvine CA USA Tech. Rep. 3. [Online]. Available: http://vision.ics.uci.edu/papers/KongF_TR_2014/KongF_TR_2014.pdf.

[28] F. Liu, J. V. Velikina, W. F. Block, R. Kijowski, and A. A. Samsonov, “Fast Realistic MRI Simulations Based on Generalized Multi-Pool Exchange Tissue Model,” *IEEE Transactions on Medical Imaging*, vol. 36, no. 2, pp. 527–537, 2017.

[29] Z. Zhan, J.-F. Cai, D. Guo, Y. Liu, Z. Chen, and X. Qu, “Fast Multiclass Dictionaries Learning With Geometrical Directions in MRI Reconstruction,” *IEEE Transactions on Biomedical Engineering*, vol. 63, no. 9, pp. 1850–1861, 2016.

[30] http://csrc.xmu.edu.cn/project/CS_MRI_FDLCP/FDLCP_EN.html.

[31] L. Feng, R. Grimm, K. T. Block, H. Chandarana, S. Kim, J. Xu, L. Axel, D. K. Sodickson, and R. Otazo, “Golden-angle radial sparse parallel MRI: Combination of compressed sensing, parallel imaging, and golden-angle radial sampling for fast and flexible dynamic volumetric MRI,” *Magnetic Resonance in Medicine*, vol. 72, no. 3, pp. 707–717, 2013.

[32] V. Papyan, J. Sulam, and M. Elad, “Working Locally Thinking Globally: Theoretical Guarantees for Convolutional Sparse Coding,” *IEEE Transactions on Signal Processing*, vol. 65, no. 21, pp. 5687–5701, 2017.

[33] S. Ruder "An overview of gradient descent optimization algorithms" [online] Available: http://sebastianruder.com/optimizing-gradient-descent/index.html#momentum.

[34] R. Chartrand, “Fast algorithms for nonconvex compressive sensing: MRI reconstruction from very few data,” *2009 IEEE International Symposium on Biomedical Imaging: From Nano to Macro*, 2009.

[35] J. Trzasko and A. Manduca, “Highly Undersampled Magnetic Resonance Image Reconstruction via Homotopic l_0-Minimization,” *IEEE Transactions on Medical Imaging*, vol. 28, no. 1, pp. 106–121, 2009.

[36] Y. Kim, M. S. Nadar, and A. Bilgin, “Compressed sensing using a Gaussian Scale Mixtures model in wavelet domain,” *2010 IEEE International Conference on Image Processing*, 2010.

Vitae

Name :Murad Almadani

Nationality :Jordanian

Date of Birth :12/31/1991

Email :murad.almadani@gmail.com

Address :Amman-Jordan

Zip Code :11953

Academic Background:

- B.S., Biomedical Engineering, 2013, Hashemite University, Zarqa, Jordan.
- M.S., Signal Processing, 2019, King Fahd University of Petroleum and Minerals, Dhahran, Saudi Arabia.

Research Interests: Biomedical Signal and Image Processing, MRI Imaging and Compressive Sensing.